JOURNAL OF PETROLOGY

Journal of Petrology, 2015, Vol. 56, No. 1, 83–112
doi: 10.1093/petrology/egu072
Original Article

OXFORD

Olivine Slurry Replenishment and the Development of Igneous Layering in a Franklin Sill, Victoria Island, Arctic Canada

Ben Hayes[1]*, Jean H. Bédard[2] and C. Johan Lissenberg[1]

[1]School of Earth & Ocean Sciences, Cardiff University, Park Place, Cardiff CF10 3AT, Uk and [2]Geological Survey of Canada, 490 De La Couronne, Québec City, Qc G1K 9A9, Canada

*Corresponding author. Telephone: 02920 874324. E-mail: hayesb@cf.ac.uk

Received May 29, 2014; Accepted November 26, 2014

ABSTRACT

The Franklin sills and dykes on Victoria Island in the Canadian Arctic represent the sub-volcanic plumbing system to the Natkusiak flood basalts, which are associated with the late Neoproterozoic (*c.* 723–716 Ma) break-up of Rodinia. The Lower Pyramid Sill (LPS) is the distal end of a sill complex that may be rooted in the Uhuk Massif, a major fault-guided magmatic feeder system. The LPS is unusual for a thin (*c.* 21 m), shallow, tholeiitic intrusion because it displays well-developed cumulate layering similar to that seen in large layered intrusions. The LPS has an aphanitic, olivine-phyric (*c.* 5%) Lower Chilled Margin (LCM), a (<1 m thick) dendritic, olivine-phyric Lower Border Zone (LBZ), a (*c.* 7 m thick) olivine-dominated (up to c. 55%) melagabbro–feldspathic-peridotite zone (OZ), a thin (*c.* 1 m) clinopyroxene-rich cumulate gabbro (CPZ) containing sector-zoned euhedral clinopyroxene, a (*c.* 10 m thick) doleritic gabbro zone (DZ), a (<1 m thick) aphyric, dendritic Upper Border Zone (UBZ) and an aphanitic, olivine-phyric (*c.* 5%) Upper Chilled Margin (UCM). Distinct compositional groups recognized in olivines from the OZ can be associated with specific crystal morphologies, some showing significant reverse zoning. Melt compositions were calculated through application of the olivine–melt Fe = Mg exchange coefficient. The calculations suggest that phenocrystic and primocrystic olivine ($Fo_{88–82}$) in the LCM–LBZ and lower OZ formed from melts with *c.* 13–10 wt % MgO. Modeling implies that reversely zoned olivine primocrysts and chadacrysts have rims in equilibrium with melts of *c.* 10–8 wt % MgO that were saturated only in olivine (+ minor chromite), whereas some olivine cores formed from melts as evolved as *c.* 6–5 wt % MgO that would have coexisted with a gabbroic assemblage. The presence of multiple olivine populations in the OZ (some reverse zoned) indicates that the LPS did not crystallize from a single pulse of melt that evolved by closed-system fractional crystallization. We propose that the reverse zoning pattern records incorporation of evolved crystals, most derived from the mushy gabbroic host, when an olivine-charged replenishment under- or intraplated the partly crystallized basaltic magma, now preserved as the DZ. The intervening CPZ may also owe its origin to the emplacement of the olivine slurry, possibly as a result of pore-scale melt mixing at this interface. The DZ shows inward differentiation trends that can be explained by *in situ* differentiation. The data imply that late emplacement of olivine-rich crystal slurries and *in situ* differentiation both played a role in the development of the layered LPS.

Key words: differentiation; Franklin; igneous layering; sill; slurry

INTRODUCTION

There is considerable petrological and geochemical evidence from active volcanoes for periodic replenishment of high-level magma chambers by the influx of new magma from depth (Murphy *et al.*, 2000; Tepley *et al.*, 2000; Garcia *et al.*, 2003; Humphreys *et al.*, 2006; Morgan *et al.*, 2006; Ginibre & Wörner, 2007). Replenishment is also well documented in layered intrusions (Wager & Brown, 1968; Huppert & Sparks, 1980; Ballhaus & Glikson, 1989; Cawthorn, 1996; Wallace & Bergantz, 2002; Namur *et al.*, 2010). Influxes of replenishing primitive magma can (1) prolong the life of a magma chamber (Usselman & Hodge, 1978; Annen *et al.*, 2014), (2) modify chemical fractionation trends (O'Hara, 1977; Dungan & Davidson, 2004; Reubi & Blundy, 2008), (3) affect the cumulate stratigraphy in layered intrusions (Wager & Brown, 1968; Cawthorn, 1996; Gibb & Henderson, 2006), and (4) trigger eruption (Brown, 1956; Sparks *et al.*, 1977; Field *et al.*, 2013). It is widely believed that primitive replenishments play a role in the formation of cyclic–macrorhythmic layering in mafic–ultramafic intrusions (Brown, 1956; Irvine & Smith, 1967; Wager & Brown, 1968; Irvine, 1977; Huppert & Sparks, 1980; Smewing, 1981).

Huppert & Sparks (1980) developed a model to explain cyclic olivine-rich–plagioclase-rich macrorhythmic layers by ponding of dense, hot, primitive magma recharges beneath a resident, more evolved basaltic magma. In the application of their model to the Rum intrusion, the contrast in composition and temperature between the two liquid layers drove vigorous convection, holding olivine in suspension in the lower layer until its eventual *en masse* deposition formed an olivine-rich macro-layer. Continuous re-equilibration with the convecting melt prior to deposition would lead to normal zoning, cause olivine compositional variations to approach end-member equilibrium crystallization paths (Tait, 1985), and explain a lack of cryptic olivine compositional variation in the Rum olivine-rich macrolayers. More recent reviews on the mechanisms of magma influx during replenishment, and the development of igneous layering, have been given by Gorring & Naslund (1995), Cawthorn (1996), Puffer *et al.* (2009) and Zieg & Marsh (2012).

Recent discussion about how large-scale cyclic–macrorhythmic olivine-rich–plagioclase-rich layering forms has been strongly polarized. One school of thought advocates the late emplacement of crystal-laden slurries into pre-existing, partly crystallized intrusions (Marsh, 2004, 2013). Another favors the emplacement of largely aphyric magmas that evolve by fractional crystallization to produce *in situ* differentiation trends (Latypov, 2009). Here we present data that bear on this debate, showing that olivine-enriched basal layers in the Franklin sills of Victoria Island formed as a result of slurry injection, much as proposed by Marsh (2004, 2013), but that the overlying gabbroic rocks are internally differentiated, as advocated by Latypov (2009) and others (Shirley, 1985; Parsons, 1987; Naslund, 1989).

Slow cooling of large intrusions allows significant post-cumulus textural (Hunter, 1996; Holness *et al.*, 2007) and compositional re-equilibration (Barnes, 1986) that may obscure primary magmatic signatures. This is especially true for olivine, owing to the rapid exchange of Fe and Mg between crystal and melt at magmatic temperatures (Chakraborty, 1997), whereas 'primary magmatic' zoning patterns of clinopyroxene (Müller *et al.*, 2013) and especially plagioclase (Grove *et al.*, 1984; Morse, 1984) seem to more commonly survive the post-cumulus stage. In contrast, thin (<100 m) intrusions would cool quickly when emplaced at shallow crustal levels (Carslaw & Jaeger, 1959) and might better preserve the textural and mineral-chemical evidence of the magmatic processes by which they formed.

The sills constituting the Neoproterozoic Franklin sub-volcanic plumbing system on Victoria Island are examples of such thin, quickly cooled systems. These sills are well exposed and unmetamorphosed, and the suite has a capping, cogenetic flood basalt sequence (Natkusiak flood basalts). The excellent preservation and availability of liquid compositions allow the physical and chemical linkages between sills, feeder or transfer dykes and the capping basalts to be established. In this study, we reconstruct the differentiation history of the Lower Pyramid Sill (LPS), a thin (*c.* 21 m) sill that is prominently layered, with an olivine-enriched lower layer and a gabbroic upper layer. Our textural and mineral-chemical observations from the LPS are best explained by mixing between a resident gabbroic mush and a late invading olivine slurry, and we propose that this is how the first-order olivine-rich–plagioclase-rich macro-layering formed.

REGIONAL GEOLOGY

The Franklin Large Igneous Province

The Franklin Large Igneous Province extends for >2500 km from the west coast of Greenland as far as the Great Bear Lake and Victoria Island in northern Canada and formed during the break-up of Rodinia as Siberia separated from northern Laurentia (Heaman *et al.*, 1992). Franklin magmatism has been dated at between *c.* 723 and 716 Ma using concordant U/Pb ages on baddeleyite–zircon from the Coronation sills and Franklin sills (Heaman *et al.*, 1992; Macdonald *et al.*, 2010). Franklin intrusions are exceptionally well exposed within the Shaler Supergroup (Rainbird *et al.*, 1996) of the Minto Inlier on Victoria Island (Fig. 1), which is a NE–SW-trending erosional window comprising intra-cratonic clastic and carbonate sediments (Jones *et al.*, 2010; van Acken *et al.*, 2013; Thomson *et al.*, 2014). The Shaler Supergroup is overlain by the Natkusiak flood basalts, a *c.* 1 km thick sequence of basaltic volcanic rocks that are related to the Franklin intrusions (Baragar, 1976; Jefferson *et al.*, 1985; Williamson

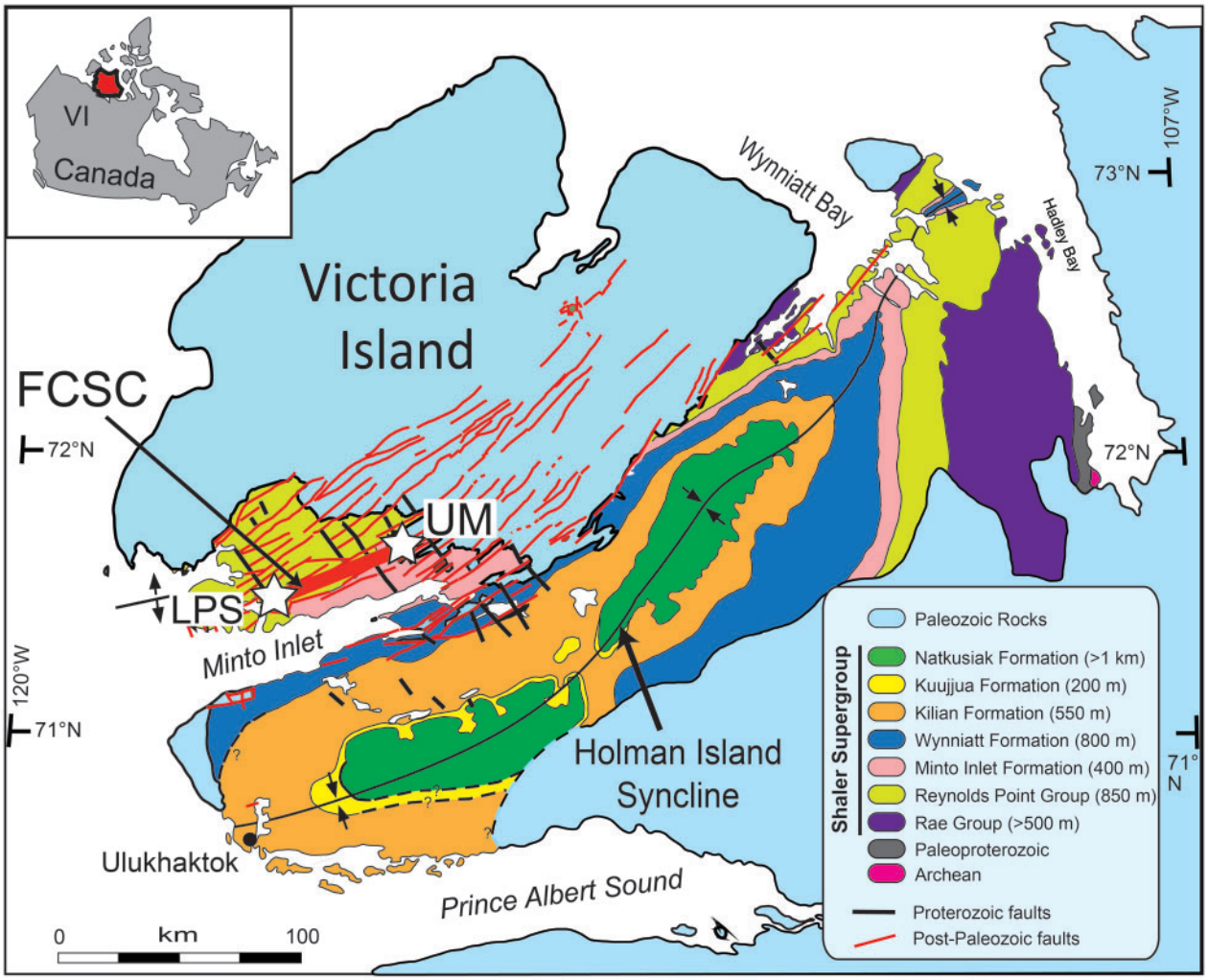

Fig. 1. Geological map of Victoria Island, modified after Thorsteinsson & Tozer (1962) and Okulitch (1992). The Lower Pyramid Sill (LPS) and the Uhuk Massif (UM) are indicated with stars and form part of the Fort Collinson Sill Complex (FCSC). The LREE–LILE-enriched populations of Type-1 sills that are locally characterized by olivine-rich bases typically occur below the Wynniatt Formation and are most common north of Minto Inlet.

et al., 2013). Franklin sills range in thickness from a few meters to *c.* 150 m, are mostly conformable to bedding and, where exposures permit, are seen to be laterally continuous for tens of kilometers along strike with little change in thickness (Bédard *et al.*, 2012). There are narrow (*c.* 2–10 m) contact metamorphic haloes around the Franklin sills (Nabelek *et al.*, 2013) with wider haloes enveloping some dykes (Hryciuk *et al.*, in preparation).

The Natkusiak flood basalts are preserved as two erosional remnants in the Holman Island syncline (Fig. 1). The lowermost extrusive unit (*c.* 50–100 m thick) is a primitive basalt (*c.* 7–11 wt % MgO) characterized by light rare earth element (LREE)–large ion lithophile element (LILE) enrichment (Bédard *et al.*, 2013). These LREE-enriched magmas are also referred to as Type-1 magmas. This lowermost extrusive unit is locally characterized by sparse olivine phenocryst pseudomorphs. Overlying this thin unit are laterally extensive basaltic (*c.* 6–10 wt % MgO) sheet flows with less strongly enriched trace element signatures (Bédard *et al.*, 2013), also referred to as Type-2 magmas. The two populations of magma compositions recognized in the volcanic sequence can be correlated with those in the underlying sills. Both magma types in the sills form gabbroic–diabasic rocks that exhibit systematic inward enrichment of FeO, TiO_2 and incompatible elements as a result of *in situ* fractional crystallization (Naslund *et al.*, 2013). The LREE–LILE-enriched sills (including the LPS) mostly occur in the lower part of the Shaler Supergroup and are commonly characterized by olivine-rich bases and gabbroic upper parts. They correspond geochemically to the lower primitive Natkusiak lavas. Sills formed from the younger, less enriched magma population lack olivine-rich layers, but may be prominently plagioclase–clinopyroxene phyric.

Lower Pyramid Sill

The LPS is located near Boot Inlet at the western end of the Minto Inlier (Fig. 1). It formed from the LREE–LILE-enriched magma population. The LPS was emplaced at a depth of *c.* 3 km based on its stratigraphic position.

It is one of many olivine-rich sills that were emplaced just above the Fort Collinson Formation quartz-arenite within a broad corridor along the Collingwood Hills. Collectively these olivine-enriched sills are known as the Fort Collinson Sill Complex (FCSC: Hayes *et al.*, in preparation). The thin (*c.* 50–100 m) Fort Collinson marker unit is embedded in much thicker sequences of dolostone and limestone, and this mechanical discontinuity appears to have greatly facilitated intrusion of the early magma pulses in the Franklin province. The western, sill-like part (*c.* 40 m thick) of the Uhuk Massif (UM), located *c.* 50 km to the east of the LPS (Fig. 1; see Bédard *et al.*, 2012), is another example of an olivine-enriched sill emplaced at this stratigraphic position. The LPS has a thin (*c.* 5–6 m) metamorphic halo surrounding it, similar to other Franklin sills (Nabelek *et al.*, 2013).

The LPS is unusual for such a thin hypabyssal intrusion in having a well-defined basal olivine-rich cumulate layer that is overlain by a sub-ophitic doleritic gabbro (Fig. 2b). The LPS has chilled contacts against a thin septum of fissile Jago Bay Formation carbonates, only a few meters above the top of the Fort Collinson quartz-arenites (Fig. 2a). The LPS (Fig. 2b) comprises an aphanitic Lower Chilled Margin (LCM), a thin (<1 m) dendrite-textured Lower Border Zone (LBZ), a *c.* 7 m thick sequence of olivine cumulate melagabbro to feldspathic-peridotite with *c.* 40–55% modal olivine (OZ), a c. 1 m thick layer of clinopyroxene-rich gabbro (CPZ), a *c.* 10 m thick layer of sub-ophitic doleritic gabbro (DZ), a thin (<1 m), dendrite-textured Upper Border Zone (UBZ) and a thin (<1 m) aphanitic Upper Chilled Margin (UCM). We have taken 26 samples from a single LPS profile with sample locations constrained by global positioning system (GPS) and height above the lower contact measured in the field (data are given in the Supplementary Data electronic appendices; supplementary data are available for downloading at http://www.petrology.oxfordjournals.org). We analysed all samples for their whole-rock major element concentrations (Fig. 2b) and 22 for mineral compositions.

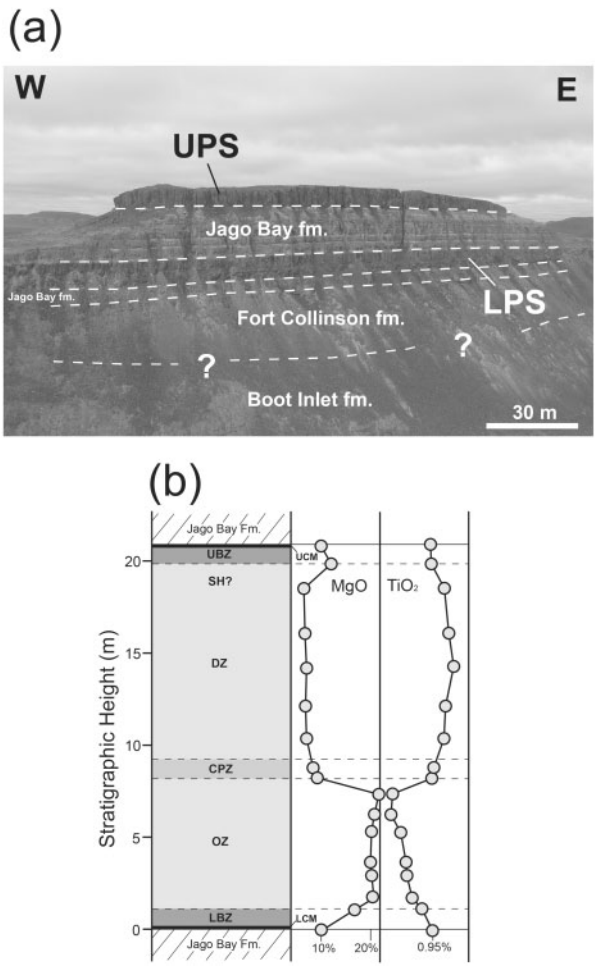

Fig. 2. (a) Photograph of the LPS showing the lower contact just above the Fort Collinson Formation quartz-rich sandstone and the upper contact against Jago Bay Formation dolostone. (b) The internal stratigraphy of the LPS showing bulk-rock variations in MgO and TiO_2 concentration (in wt %).

ANALYTICAL METHODS

Whole-rock analysis

Rock samples were reduced to powder in the rock preparation laboratory of Cardiff University. Each sample was crushed to coarse grit using a steel jaw crusher before 80 g of each sample was milled in an agate planetary ball mill to a fine powder. Afterwards, 2 g of each powdered sample was ignited for 2 h in a furnace at 900°C to burn off volatile substances and determine loss on ignition (LOI) values. The samples were then put into solution for inductively coupled plasma optical emission spectrometry (ICP-OES) and inductively coupled plasma mass spectrometry (ICP-MS) analysis using the lithium metaborate fusion method (McDonald & Viljoen, 2006). The instruments used at Cardiff University to analyse element abundances were a Jobin Horiba Ultima 2 ICP-OES system and a Thermo Elemental ZT series ICP-MS system. The full whole-rock dataset is included in the Supplementary Data electronic appendices.

Electron microprobe

In situ mineral chemical analyses were carried out using a Cameca SX-100 electron microprobe at Laval University in Québec City, Canada. The probe was fitted with five wavelength-dispersive spectrometers. All phases were analysed on polished thin sections using a focused beam (1 μm diameter), 20 nA current and a 15·0 kV accelerating potential. Counting times were typically 30 s on peak and background levels. Core to rim profiles were carried out on the major silicate phases. Where grain size was very fine or only a representative core composition was required, spot analyses were obtained. The dataset for each phase analysed and the analytical conditions for each mineral species are supplied in the Supplementary Data electronic appendices.

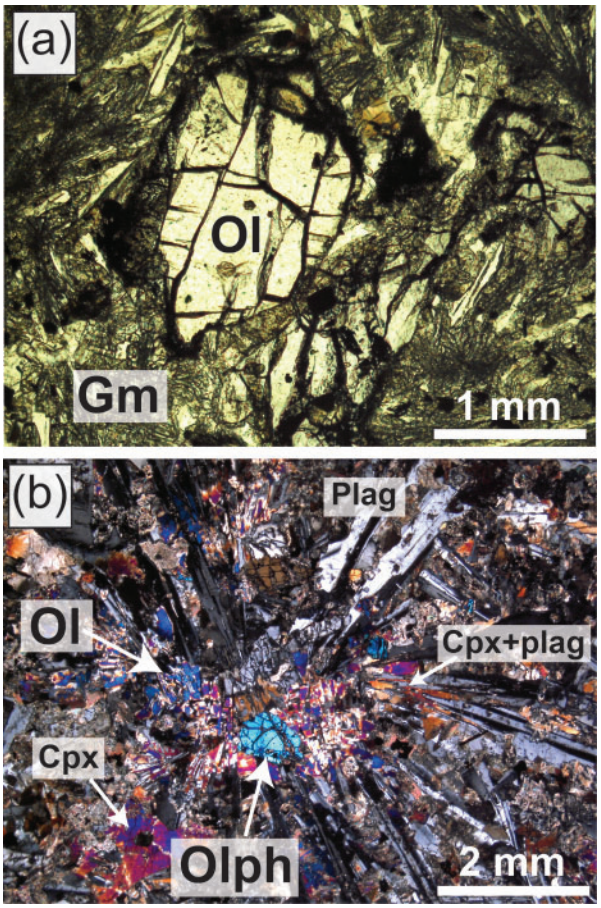

Fig. 3. Photomicrographs of LCM and LBZ textures. (a) At the lower contact with the Jago Bay Formation, euhedral olivine (Ol) phenocrysts occur in a fine-grained, quenched groundmass (Gm) (image in plane-polarized light). (b) Within the LBZ, *c.* 20 cm above the lower contact, the quenched groundmass grades into coarser dendrites of plagioclase (Plag) and clinopyroxene (Cpx) that cement olivine phenocrysts (Olph). Olivine (Ol) is also intergrown with the dendrites, suggesting that the melt reached the three-phase cotectic early in its crystallization history (image in crossed Nicols).

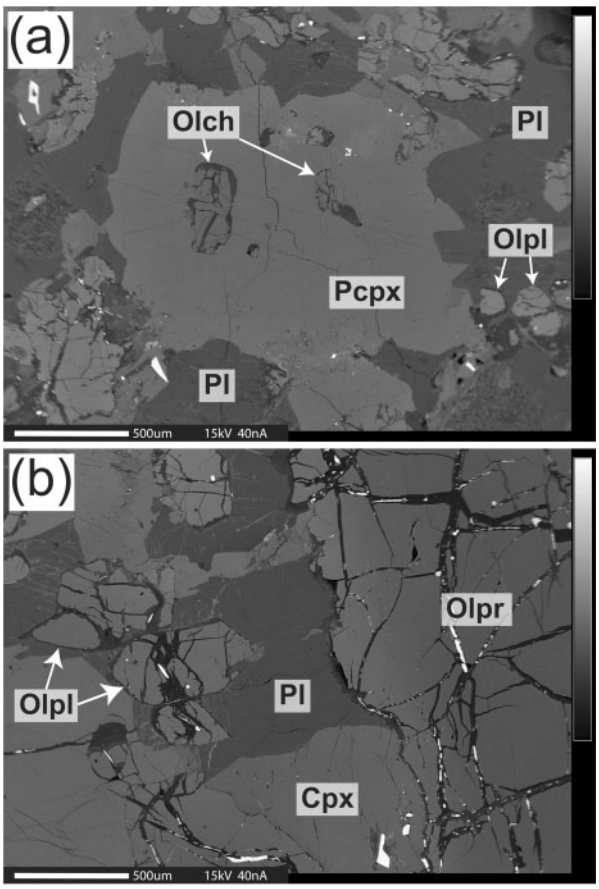

Fig. 4. Backscattered electron (BSE) images showing LOZ olivine morphologies. (a) A clinopyroxene oikocryst (Pcpx) encloses olivine chadacrysts (Olch) and is surrounded by anhedral, interstitial plagioclase (Pl), which encloses groundmass olivines (Olpl). (b) Euhedral and clustered groundmass olivines (Olpl) enclosed by anhedral, interstitial plagioclase (Pl). The edge of a large, normally zoned olivine primocryst (Olpr) is also visible.

PETROGRAPHY

Lower Chilled Margin (LCM)

The LCM (sampled at *c.* 5 cm above the contact) has ≤5% euhedral olivine phenocrysts (*c.* 0·5–2 mm), which may contain tiny chromite microphenocrysts as inclusions. The olivine phenocrysts are surrounded by a fine-grained (*c.* 0·1 mm) groundmass (Fig. 3a) that grades from massive aphanitic material to a felted mass of dendritic plagioclase and clinopyroxene.

Lower Border Zone (LBZ)

In the LBZ, the proportion of olivine phenocrysts (*c.* 1–2 mm, also with minor Cr-spinel inclusions) increases to *c.* 10–15% (at *c.* 20 cm above the lower contact). The dendritic intergrowths of plagioclase and clinopyroxene reach *c.* 2 mm grain sizes with dendrites commonly nucleating on the surface of olivine phenocrysts (Fig. 3b). The rims of some olivine crystals are intergrown with the plagioclase–clinopyroxene dendrites, suggesting that the three phases co-saturated during crystallization of the LBZ (Fig. 3b). The textures, with the presence of cumulus olivine, are consistent with a weakly olivine-cumulative composition for the LBZ.

Olivine Zone (OZ)

There is a noticeable textural change *c.* 1 m above the lower contact of the LPS. At this height, modal olivine increases over a few centimeters to *c.* 40% and the groundmass texture changes from dendritic to medium-grained poikilitic (Fig. 4a). We define this modal and textural transition as the boundary between the LBZ and the OZ. The OZ is *c.* 7 m thick and is composed of cumulate olivine melagabbro to feldspathic-peridotite. Cr-spinel microphenocrysts are present throughout the OZ, typically as inclusions in olivine primocrysts and as grains embedded in interstitial clinopyroxene and plagioclase.

Olivine within the OZ can be broadly assigned to four textural groups: (1) euhedral olivine primocrysts (*c.* 0·5–2 mm), which commonly contain euhedral

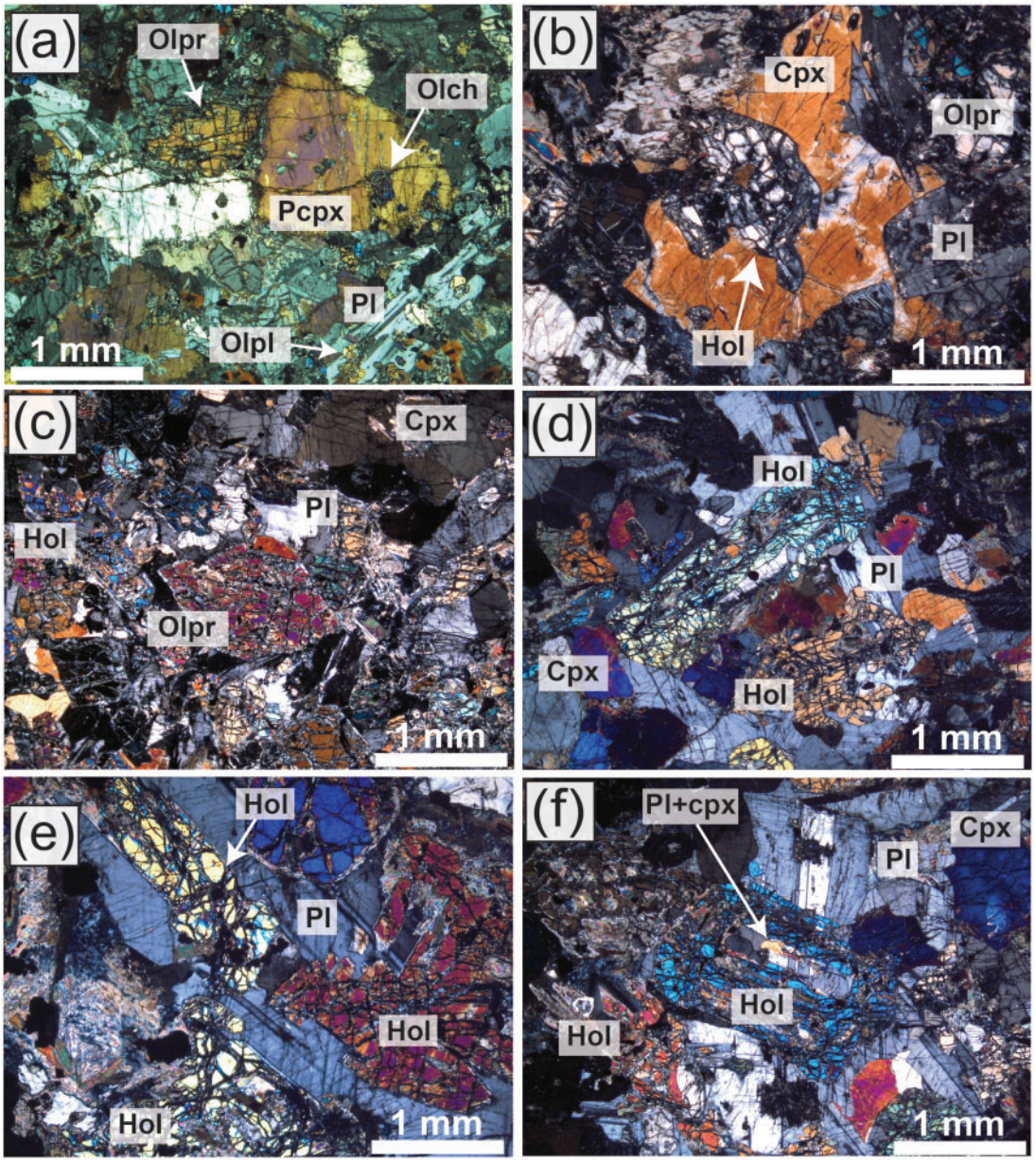

Fig. 5. Photomicrographs of OZ textures (all with crossed Nicols). (a) LOZ showing an olivine primocryst (Olpr) and poikilitic clinopyroxene (Pcpx), which encloses smaller olivine chadacrysts (Olch). Finer grained olivine crystals (Olpl) can also be seen, surrounded by interstitial plagioclase (Pl). (b) MOZ showing a hopper olivine (Hol), which is overgrown by clinopyroxene (Cpx). (c) Image showing the abundant olivine of the MOZ, with olivine primocrysts (Olpr) and hopper olivines (Hol). (d) Hopper olivines (Hol) in the UOZ. (e) UOZ hopper olivines (Hol) that are intergrown with interstitial plagioclase (Pl). (f) UOZ hopper olivine (Hol) that appears to enclose plagioclase and clinopyroxene (Pl + cpx). Euhedral clinopyroxene crystals (Cpx) are also present, as well as interstitial plagioclase (Pl).

Cr-spinel microphenocrysts (Fig. 5a and c); (2) chadacrystic fine-grained (*c.* 0·2–0·5 mm) euhedral–subhedral olivine crystals (some bearing Cr-spinel inclusions), which are enclosed by clinopyroxene oikocrysts (Figs 4a, 5a and 6f); (3) fine-grained (*c.* 0·2–0·5 mm) groundmass olivine crystals (some bearing Cr-spinel inclusions) surrounded by interstitial plagioclase (Figs 4b, 5a and 6f); (4) hopper olivines (*c.* 0·2–2 mm), which are skeletal in habit in cross-section and orthorhombic in basal sections, where they appear to enclose clinopyroxene and plagioclase (Fig. 5d–f). Hopper olivines also have anhedral margins indicating co-crystallization with plagioclase (Fig. 5d and e). We subdivide the OZ based on the spatial distribution of these olivine textures into three subzones: lower (LOZ), middle (MOZ) and upper (UOZ) olivine zone. The LOZ consists of a basal pyroxene-poikilitic olivine-melagabbro, which mainly consists of euhedral olivine primocrysts, olivine chadacrysts and groundmass olivines (Figs 4a, 5a and 6f), with only minor (*c.* 5%) proportions of fine-grained (<0·5 mm) hopper olivine. The MOZ is dominated by hopper olivine crystals that are typically intergrown with clinopyroxene, with subordinate primocrystic, chadacrystic, and groundmass olivine (Fig. 5b and c). The

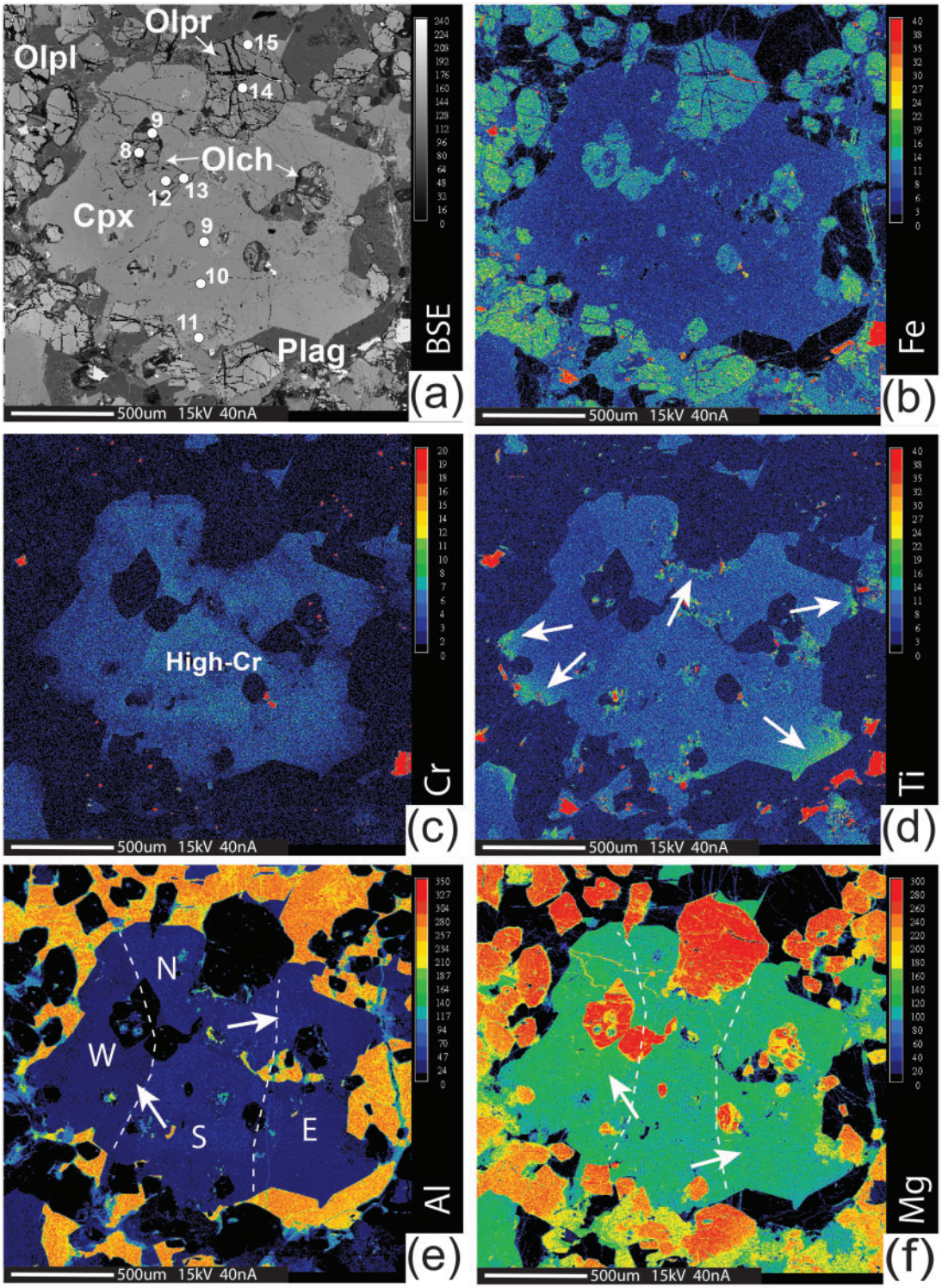

Fig. 6. Back-scattered electron (BSE) image (a) and element maps (b–f) of a clinopyroxene oikocryst from the LOZ with olivine chadacrysts ($Fo_{83–81}$). (a) BSE image showing analysis spots and numbers (clinopyroxene core composition is Mg# 85). (b) Fe, (c) Cr, (d) Ti, (e) Al, and (f) Mg element maps. The clinopyroxene oikocryst appears to display sector-zoning, visible in the Mg and Al element maps. It also has a narrow Fe–Ti-enriched rim [indicated with white arrows in (d)]. The interstitial nature of plagioclase is visible in (e). The Fe-rich groundmass olivines are hosted by interstitial plagioclase. N, north; S, south; E, east; W, west.

UOZ is dominated by hopper olivine morphologies with subordinate euhedral primocrystic and groundmass olivine, and few olivine chadacrysts hosted by poikilitic clinopyroxene (Fig. 5d–f).

Clinopyroxene (*c.* 1–2 mm) habits range from euhedral to subhedral in the LOZ and it commonly encloses olivine chadacrysts (Figs 4a and 6). Clinopyroxene becomes more subhedral to anhedral in the MOZ, where

intergrowths with olivine are common (Fig. 5b). In the UOZ, euhedral cumulus clinopyroxene crystals appear (*c*. 1–2 mm; Fig. 5d and f), substituting for the clinopyroxene oikocrysts that typify the LOZ and the anhedral clinopyroxenes present in the MOZ. Subordinate intergranular, interstitial clinopyroxene occurs throughout the OZ.

Plagioclase is anhedral throughout the OZ and is interstitial to cumulus olivine (Figs 4b and 6) and mostly interstitial to clinopyroxene, except for local co-crystallization textures (Fig. 5b, d and e). There are minor accessory amphibole and biotite, and there are traces of groundmass Fe–Ti oxides and Fe–Ni–Cu sulphides.

Clinopyroxene Zone (CPZ)

The CPZ is *c*. 1 m thick. The diffuse base of the CPZ is characterized by a drop in the mode of olivine to *c*. 5% and a corresponding increase in the proportion of euhedral cumulus clinopyroxene to *c*. 30–40% (*c*. 0·5–1 mm). The euhedral clinopyroxene crystals are often sector-zoned (Fig. 7) and are distributed as trains of grains (Fig. 8), reminiscent of those described by Philpotts *et al*. (1998). Between these trains of sector-zoned clinopyroxene is a gabbroic matrix consisting of serpentinized olivine (*c*. 5%), euhedral–subhedral clinopyroxene and interstitial plagioclase with subordinate interstitial clinopyroxene. There is minor (<5%) magnetite and ilmenite, as well as accessory amphibole and biotite.

Dolerite Zone (DZ)

The DZ is characterized by the absence of olivine and modal increases in plagioclase (from *c*. 25% in the OZ to 40% in the DZ) and clinopyroxene (from *c*. 30% in the OZ to *c*. 40% in the DZ). The DZ is also marked by a change in the morphology of plagioclase, from subhedral–anhedral interstitial textures to coarser (*c*. 2–3 mm) lath-shaped crystals that mostly form ophitic intergrowths with clinopyroxene. Around 5–10% of the plagioclase–clinopyroxene mode is composed of cumulus crystals that do not display intergrowth textures. Full thin section scans show domains of sub-ophitic dolerite with varying grain sizes (vari-textured), with coarser pegmatitic patches (*c*. 5 mm plagioclase and *c*. 3–4 mm clinopyroxene) and finer-grained domains (*c*. 2–3 mm plagioclase and *c*. 1–2 mm clinopyroxene) present in the DZ.

Clinopyroxene is typically euhedral–subhedral and intergrown with plagioclase, but both augite and low-Ca pigeonite also occur as separate cumulus crystals. Low-temperature alteration is more common in the DZ compared with other zones of the LPS, with plagioclase and clinopyroxene being partly altered to fine-grained albite and saussurite, or chlorite and actinolite (respectively). This is interpreted to represent deuteric alteration caused by volatile exsolution during the final stages of LPS crystallization. Olivine was not observed in the DZ, but sparse orthopyroxene grains (*c*. 5–10%) in the lower DZ may be pseudomorphous after olivine. Interstitial ilmenite and magnetite are present (*c*. 5–10%), as are interstitial sulphides (*c*. 5%), with associations of pyrrhotite–pyrite in the lower DZ grading into associations of pyrite–chalcopyrite in the upper DZ. Minor accessory amphibole and biotite occur throughout the DZ and may be associated with interstitial granophyre in the uppermost DZ (*c*. 19–20 m height). Also, in the uppermost DZ, long (*c*. 5–10 mm), blade-like clinopyroxene crystals are present with preferred growth directions roughly perpendicular to the upper contact of the LPS (element maps are included in the Supplementary Data electronic appendices).

Upper Border Zone (UBZ)

The UBZ (from *c*. 20 m to *c*. 21 m height) consists largely of fine-grained (<1 mm) plagioclase and clinopyroxene dendrites. There are also coarser subhedral–anhedral clinopyroxene grains (*c*. 1–2 mm), which show both sector-zoning and complex concentric zoning, locally with sieve-textures. No olivine phenocrysts (nor their pseudomorphs) were observed in the UBZ.

Upper Chilled Margin (UCM)

The LPS at its upper contact with the Jago Bay Formation carbonate is similar to the LCM in that it is a very fine-grained, almost glassy, chilled contact. It contains *c*. 5% olivine phenocrysts (*c*. 1–2 mm) that have been completely pseudomorphed by secondary serpentine. The groundmass appears to consist of very fine-grained dendrites, but it is more altered in comparison with the LCM. A few amygdales (<5%; *c*. 2 mm) are filled with biotite and chlorite.

MINERAL CHEMISTRY

The main silicate phases present in each layer in the LPS were analysed by electron microprobe. Chemical zonations were mapped to constrain the crystallization history of the LPS. We use the term 'core' when referring to the central region of a crystal, 'mantle' for the intermediate part between the core and rim (often with weak compositional gradients) and 'rim' for the strongly zoned edges of a crystal. We use 'primocryst' when we refer to euhedral cumulus crystals, which are typically ≥1 mm in size, and 'phenocryst' for euhedral crystals in the chills and border zones.

Olivine

Compositional variations of olivine in the LCM, LBZ and OZ are summarized in Fig. 9. Variations in Fo content [molar Fo = 100 Mg/(Mg + Fe^{2+})] are typically correlated with olivine NiO (wt %) contents.

Olivine phenocrysts in the LCM are normally zoned with near-constant core and mantle compositions and narrow, more evolved rims. The average core and rim compositions are Fo_{87} and Fo_{82}, respectively. The cores and mantles of olivine phenocrysts in the LCM have an average NiO content of 0·32 wt %, whereas the rims have a lower NiO content of 0·28 wt %. Some euhedral olivine phenocrysts show subtle core to mantle

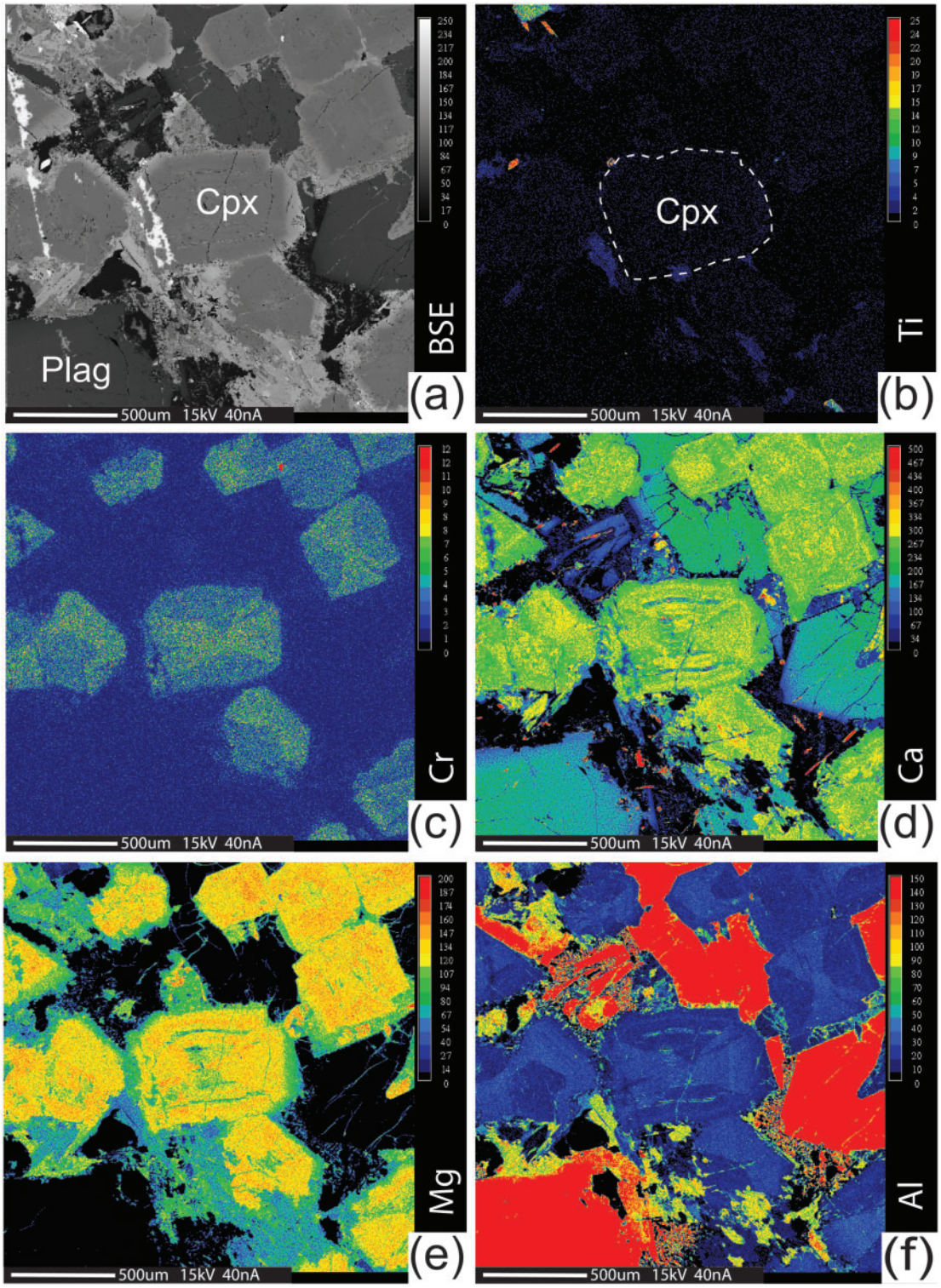

Fig. 7. BSE (a) and element maps (b–f) of sector-zoned clinopyroxenes from the CPZ. (a) BSE image. (b) Ti, (c) Cr, (d) Ca, (e) Mg, and (f) Al element maps. The hourglass style sector-zoning is characterized by zones with 2–3 times more enrichment in both Cr and Al.

increases in Fo content (*c.* 0·3–0·4 mol % increases) followed by decreasing Fo at the rim. A small olivine phenocryst in the LCM displays unusually strong zoning from Fo_{86} (0·28 wt % NiO) in the core to Fo_{75} (0·24 wt % NiO) at its rim.

In the LBZ, the average core composition of olivine phenocrysts is Fo_{85} (0·29 wt % NiO). Olivine commonly shows strong normal zoning with an average rim composition of Fo_{75} (0·2 wt % NiO). Locally, some olivine phenocrysts in the LBZ show weak reverse zoning from

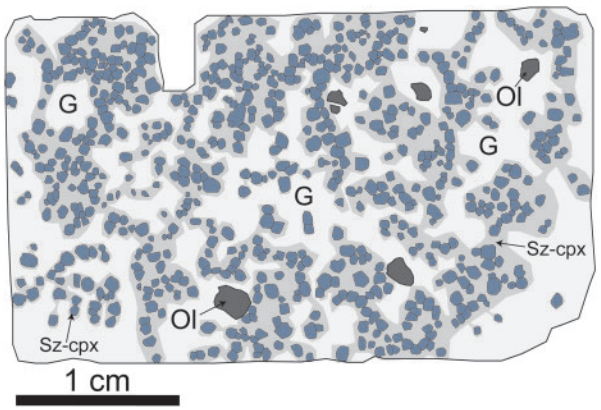

Fig. 8. Digitized image of a thin section from the CPZ (*c.* 8 m), showing how the sector-zoned clinopyroxene (Sz-cpx) defines 'trains'. The lighter grey is the gabbroic matrix (G), consisting of cumulus clinopyroxene (+low-Ca pigeonite), interstitial plagioclase and minor (<5%) Fe–Ti oxides; the matrix also includes minor (*c.* 5%) olivine (Ol), which has been completely serpentinized. The darker grey areas surrounding the sector-zoned clinopyroxenes, outline the morphology of these 'trains'.

core to mantle (*c.* 1 mol %), but with little corresponding change in NiO content (average *c.* 0·32 wt %).

In the LOZ, olivine primocrysts have core compositions ranging between Fo_{88} and Fo_{82} (0·4–0·25 wt % NiO). Smaller olivine chadacrysts (enclosed by clinopyroxene oikocrysts) have systematically lower Fo contents and a restricted range of compositions with an average core composition of Fo_{83} (0·25 wt % NiO) and an average rim composition of Fo_{81} (0·2 wt % NiO). Groundmass olivine surrounded by plagioclase has still more evolved compositions with average core and rim compositions of Fo_{81} (0·21 wt % NiO) and Fo_{70} (0·1 wt % NiO), respectively. Most olivines in the LOZ are zoned. The larger olivine primocrysts commonly exhibit normal zoning with near-constant core and mantle compositions, and narrow Fe-rich rims as evolved as $Fo_{77–75}$. Chadacrystic olivines enclosed by clinopyroxene oikocrysts are mostly normally zoned (typically a *c.* 1–2 mol % change from core to rim) except for a weakly reverse-zoned olivine grain that has a core composition of Fo_{82} (0·2 wt % NiO) that increases to Fo_{83} (0·24 wt % NiO) at its rim. Groundmass olivines that are surrounded by plagioclase are generally normally zoned and reach very low Fo compositions at the rims (*c.* $Fo_{77–70}$), but may also show weak reverse zoning with core to rim increases of *c.* 0·5 mol % (with NiO contents <0·2 wt % for both core and rim).

In the MOZ and UOZ, the relative proportion of olivine primocrysts decreases, whereas the total olivine mode increases (up to *c.* 55%). Olivines enclosed by clinopyroxene oikocrysts become less common, but where present they have a restricted compositional range ($Fo_{83–81}$). In the MOZ, the average Fo composition of groundmass olivines is generally more primitive (*c.* Fo_{80}) than the average groundmass olivines from the LOZ (*c.* Fo_{75}). Subtle (*c.* 1 mol %) reverse zoning is observed in both groundmass and hopper olivines in the MOZ.

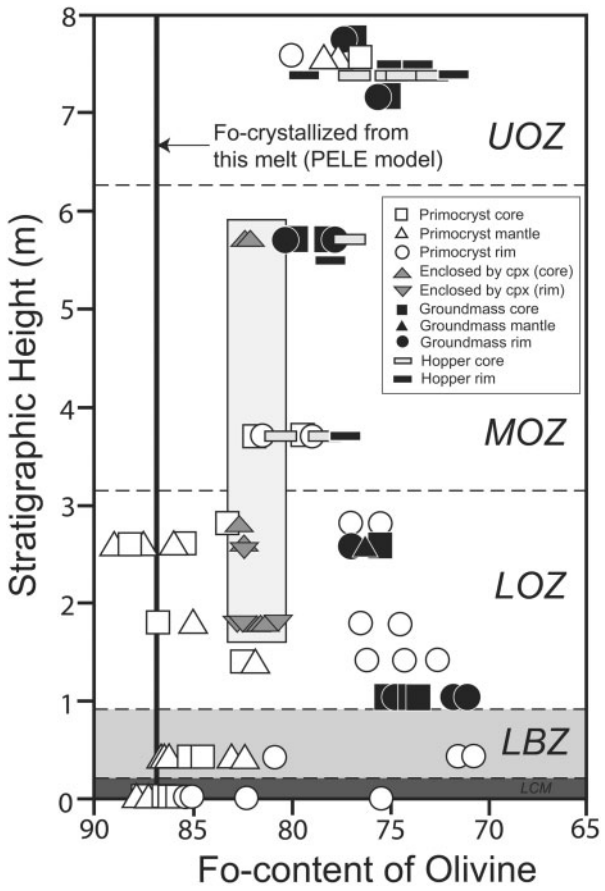

Fig. 9. Stratigraphic column showing olivine compositional variations in molar forsterite (Fo) content through the LCM, LBZ and OZ, the latter subdivided into a lower, middle and upper OZ (LOZ, MOZ, and UOZ, respectively). The grey shaded rectangle indicates the compositional range of olivines that are enclosed by clinopyroxene, which is tightly clustered around $Fo_{83–81}$. 'This melt' refers to the LPS chill composition.

In the UOZ, common hopper olivines have core compositions as low as Fo_{73} and commonly display reverse zoning with rims between Fo_{80} and Fo_{77}. An olivine primocryst in the UOZ displays reverse zoning (Fig. 10), with a core to rim increase from Fo_{77} (0·16 wt % NiO) to Fo_{80} (0·23 wt % NiO). Groundmass olivine in the UOZ shows reverse zoning for Fo, with cores of *c.* Fo_{77} and rim compositions ranging between Fo_{80} and Fo_{78} (with NiO content for core and rim typically <0·22 wt %).

Cr-spinel

Cr-spinel microphenocrysts enclosed by phenocrystic olivine in the LCM have compositions that depend on their location in the host olivine phenocryst. For example, a Cr-spinel in the core of an olivine phenocryst has a Cr# [$= 100Cr/(Cr + Al)$] of 50, whereas a Cr-spinel included in the rim of the same olivine has a higher Cr# of 58. Neither Fe3# [$= 100Fe^{3+}/(Fe^{3+} + Cr + Al)$] nor Fe2# [$= 100Fe^{2+}/(Mg + Fe^{2+})$] for these LCM Cr-spinel microphenocrysts shows any variation, however.

Cr-spinels inclusions in the LOZ have very similar compositions (Cr# 73–46; Fe3# 18–10; Fe2# 84–41) to

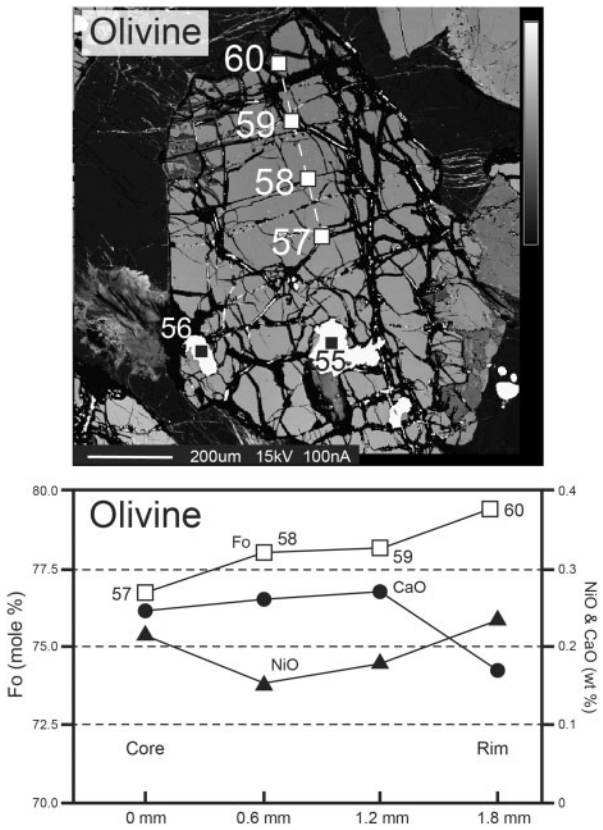

Fig. 10. BSE image and corresponding electron microprobe traverse of an olivine primocryst from the UOZ. Spot analysis numbers are indicated (open squares) and correspond to the microprobe traverse. The spot analysis numbers for the Cr-spinel inclusions (black squares) are also shown. Data are given in the Supplementary Data electronic appendices. The olivine is reversely zoned, with increasing Fo content towards its rim (increasing from Fo_{77} to Fo_{80}), as well as increasing NiO (wt %) and decreasing CaO (wt %) at the rim.

those of the LCM–LBZ. Conversely, Cr-spinels show more significant compositional variations in the UOZ. For example, a Cr-spinel in the core of a reversely zoned UOZ olivine primocryst (Fo_{77}; Fig. 10) has a Cr# of 67, Fe3# of 67 and Fe2# of 84, whereas the Cr-spinel located in the olivine rim (Fo_{80}; Fig. 10) has a higher Cr# of 71, and markedly lower Fe3# of 59 and a lower Fe2# of 80.

Clinopyroxene

The variation of Mg# [molar Mg# = 100 Mg/(Mg + Fe^{2+} + Mn)] of clinopyroxene versus stratigraphic height is summarized in Fig. 11. The Mg# of groundmass clinopyroxene in the LBZ is relatively low (Mg# 77–70) compared with clinopyroxenes of the overlying OZ. Most LBZ clinopyroxene crystals are normally zoned (decreasing Mg# towards the rims), but some are reversely zoned, with Mg# increasing by up to *c.* 3 mol % towards the rim (Fig. 12b).

In the OZ, clinopyroxene core compositions show little variation with stratigraphic position (Fig. 11) with Mg# 86–83 and average Cr_2O_3 of *c.* 0·8 wt % and average TiO_2 of *c.* 0·4 wt % (Figs 12a and 13). Clinopyroxene oikocrysts have near-constant core–mantle compositions (Fig. 12a), but may have narrow Fe–Ti-rich rims (Mg# *c.* 75; Fig. 12a; also see Fig. 6b and d). The evolved rim compositions of oikocrystic and cumulus clinopyroxene in the OZ overlap with the compositions of interstitial OZ clinopyroxene, and with those of LBZ groundmass clinopyroxene (Fig. 11). Some LOZ clinopyroxene oikocrysts show subtle sector-zoning, visible on element maps of Cr, Al and Mg (Fig. 6c–f); Cr and Al (Fig. 6c and e) appear to show similar behaviour and are slightly enriched in the north–south sector, whereas Mg (Fig. 6f) is more enriched in the east–west sector of the clinopyroxene.

In the CPZ, euhedral cumulus clinopyroxenes, which are often sector-zoned, have core compositions similar to those of OZ clinopyroxene (Mg# *c.* 83; Fig. 11), whereas rims extend to compositions that are more Fe-rich (Mg# 70–30) than clinopyroxene rims in the underlying OZ. The sector-zoning of clinopyroxene is apparent on element maps (Fig. 7), with different zones showing weak contrasts in Cr and Al abundance (Fig. 7c and f), whereas Ca and Mg show no clear inter-zone differences (Fig. 7d and e). Cr_2O_3 typically decreases from *c.* 0·6 wt % in the cores to *c.* 0·2 wt % in the rims, whereas Al_2O_3 increases from *c.* 1·8 wt % in the cores to *c.* 2 wt % at the rims. TiO_2 contents also increase slightly from the cores (*c.* 0·4 wt %) to the rims (*c.* 0·5 wt %), which contrasts with the much greater increase in TiO_2 (to *c.* 1 wt %) seen in OZ clinopyroxene rims. We suspect that the deficit in TiO_2 of CPZ clinopyroxene rims may be due to sequestration of TiO_2 into interstitial ilmenite in the case of the CPZ. The CPZ grades upward over *c.* 0·8 m into slightly more evolved clinopyroxene core compositions (Mg# 80), which have reversely zoned mantles (up to Mg# 83), suggesting interaction with a more MgO-rich melt. The presence of wide, strongly evolved rims on all forms of clinopyroxene in the CPZ suggests that all have interacted with abundant, late, evolved pore melts during the final stages of crystallization, possibly suggesting higher trapped melt fractions in these rocks.

In contrast to the muted variations of clinopyroxene compositions in the OZ, clinopyroxene in the DZ shows systematic up-section cryptic variations (Fig. 11). At the base of the DZ, clinopyroxene compositions overlap with those of clinopyroxene from the OZ and CPZ (Mg# *c.* 84). A cumulus-textured clinopyroxene at the base of the DZ (Fig. 14a) shows complex zoning, with a core composition of Mg# 84 that increases outward gradually to Mg# 85 and then shows a sudden decrease out to Mg# 63 in the rim. This pattern of Mg-enrichment in the mantle of cumulus clinopyroxene occurs sporadically in the DZ (Fig. 11). More generally, clinopyroxene displays strong normal core to rim zoning throughout the DZ with changes in Mg# ranging between *c.* 10 and 20 mol %. Rims of euhedral clinopyroxene overlap with the compositions of evolved interstitial clinopyroxene in the DZ. Interstitial clinopyroxene from the DZ is more evolved than interstitial clinopyroxene from the OZ.

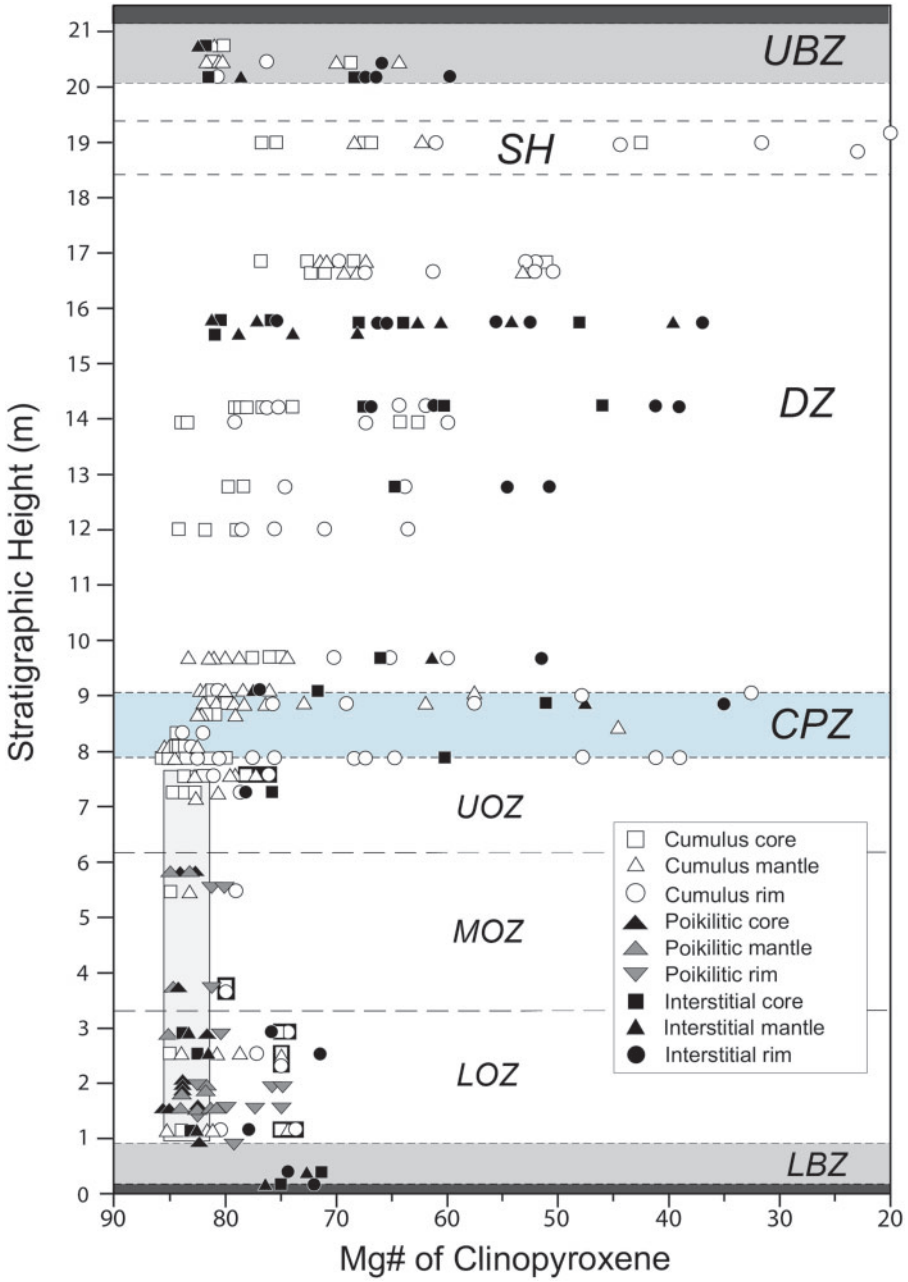

Fig. 11. Stratigraphic column showing clinopyroxene compositional variations in molar magnesium number [Mg# = 100 Mg/(Mg + Fe^{2+} + Mn)] through the LPS. The grey shaded rectangle in the OZ indicates the range of poikilitic and cumulus clinopyroxene core compositions in the OZ (between Mg# 85 and 82), illustrating the restricted range in composition.

In the upper DZ, clinopyroxenes (including bladed clinopyroxene crystals) have core compositions of Mg# 75–70 and strong normal zoning at the rims (to Mg# 30–20). The peak in clinopyroxene Fe-enrichment, just below the UBZ, may represent a type of 'sandwich' horizon.

The UBZ contains a rare, euhedral (*c.* 1 mm), sector-zoned clinopyroxene with compositions of Mg# 81 in the crystal core (Fig. 14b), with a narrow Fe–Ti-enriched rim (element maps of this crystal are included in the Supplementary Data electronic appendices). This crystal is sieve-textured with mantle depletion in Mg# (Mg# 70–67; Fig. 14b) relative to the rims, which may indicate a thermal spike, or a reaction with more primitive melt. Interstitial clinopyroxene is intergrown with plagioclase and has evolved compositions (Mg# *c.* 67).

Plagioclase

Plagioclase anorthite [An; molar An = 100Ca/(Ca + Na + K)] content versus stratigraphic height is shown in Fig. 15. Plagioclase dendrites within the LCM groundmass have relatively low An values, averaging An_{64}. In the LBZ, the coarser plagioclase dendrites become slightly more primitive with compositions of *c.* An_{71}.

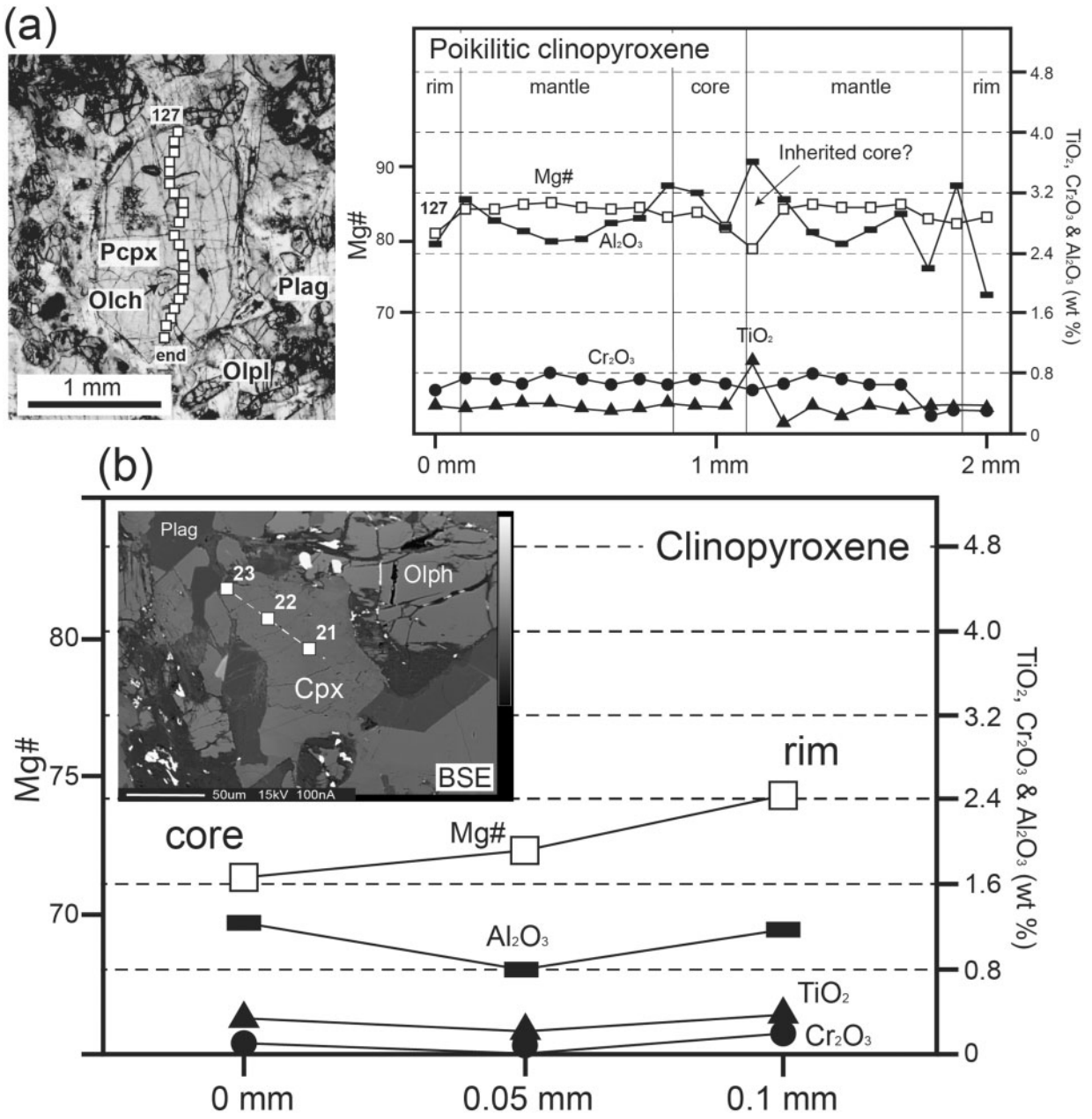

Fig. 12. (a) A poikilitic clinopyroxene crystal (Pcpx: *c.* 1·5 mm) from the LOZ (plane-polarized light photomicrograph), with the corresponding microprobe traverse. The profile starting at No. 127 traverses the crystal in a north–south direction and avoids the olivine chadacrysts (Olch). The clinopyroxene is normally zoned with narrow rims. (b) BSE image of a subhedral (interstitial?) clinopyroxene (Cpx) from the LBZ, which is adjacent to an olivine phenocryst (Olph). The corresponding microprobe traverse exhibits increasing Mg# towards its rim (i.e. reverse zoning).

Plagioclase has core compositions of $An_{73–68}$ throughout the OZ. Most grains show normal zoning with sporadic occurrences of reverse zoning. Plagioclase rim compositions extend to An contents as low as An_{58}, with the lowest An values adjacent to olivine crystals. Core compositions of interstitial plagioclase in the CPZ (Fig. 16a) are between An_{72} and An_{70}, whereas rims are strongly evolved (*c.* An_{40}). CPZ plagioclase core compositions overlap the composition of OZ plagioclase. In the CPZ, minor euhedral cumulus plagioclase is more primitive with core and mantle compositions up to An_{76}.

Plagioclase core and mantles are typically *c.* $An_{70–60}$ in the DZ, with strongly evolved rims as low as An_{45}. Rare, cumulus-textured plagioclase in the lower DZ has some of the most primitive An compositions ($An_{77–76}$; Fig. 16b) in the LPS. In some plagioclase crystals in the middle DZ, the cores are mantled by higher An plagioclase, suggesting interaction with a more primitive melt prior to the initiation of *in situ* fractional crystallization. The core and rim compositions with the lowest An values occur in the upper DZ (Fig. 15) where clinopyroxene has the lowest Mg# (Fig. 11), corresponding to the inferred position of the sandwich horizon.

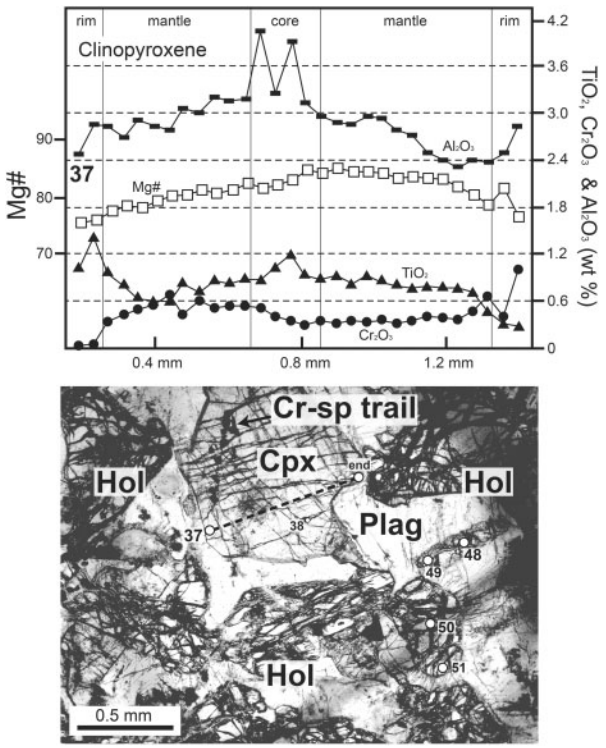

Fig. 13. Electron microprobe traverse across a subhedral clinopyroxene (Cpx) crystal (No. 37) from the UOZ, which is surrounded by interstitial plagioclase (Plag). The corresponding photomicrograph is in plane-polarized light. The clinopyroxene is normally zoned with narrow Fe-enriched rims. Cr_2O_3 (wt %) shows increases towards one rim, but decreases towards the other. A small hopper olivine (Hol; Nos 48 and 49) surrounded by plagioclase shows reverse zoning (core $Fo_{77·6}$ to rim $Fo_{79·5}$). Data are given in the Supplementary Data electronic appendices.

A fine-grained (*c.* 0·2 mm) plagioclase dendrite in the UBZ is reversely zoned at its rim (Fig. 17) and, as for clinopyroxene (Fig. 14b), may record a temperature increase and/or a primitive replenishment event.

CALCULATED MELT CHEMISTRY

The Fe/Mg ratio of a crystal can be used to calculate the Fe/Mg of its equilibrium melt if the Fe = Mg exchange coefficient is known (e.g. Roeder & Emslie, 1970). Data from Franklin sill chilled margins and the coeval Natkusiak flood basalts were used to parameterize covariations of melt Fe/Mg ratio with melt MgO, allowing melt MgO in equilibrium with both olivine and clinopyroxene to be calculated.

Olivine

An exchange coefficient (K_d) of 0·34 as experimentally determined by Matzen *et al.* (2011) was used to calculate the exchange of molar FeO and molar MgO between olivine and melt. The cores and mantles of euhedral olivine phenocrysts in the LCM yield model melts with up to *c.* 13 wt % MgO. The narrow evolved rims on these grains yield model melts of *c.* 11–10 wt % MgO, closer to the LPS chill composition. The most evolved olivine phenocryst rims yield model melts of *c.* 6·5 wt % MgO. In the LBZ, phenocrystic olivines have cores equivalent to model melts of *c.* 11 wt % MgO, and have narrow, Fe-rich rims equivalent to model melts of *c.* 5 wt % MgO.

Olivine primocryst cores from the LOZ yield model melts between *c.* 13·5 and 10 wt % MgO, whereas their rims yield a melt range of *c.* 8–6 wt % MgO. Olivine chadacrysts enclosed by clinopyroxene oikocrysts yield magnesian model melts between *c.* 10 and 8·5 wt % MgO. A reversely zoned olivine chadacryst has a core in equilibrium with a model melt of 9·8 wt % and a rim in equilibrium with a model melt of 10·2 wt % MgO. Groundmass olivines in the LOZ are in equilibrium with model melts ranging between *c.* 7 and 5 wt % MgO. In the UOZ, primocrystic olivine and hopper olivine cores yield evolved model melts ranging between *c.* 8 and 5 wt % MgO. A reversely zoned olivine primocryst (Fig. 10) in the UOZ has a core in equilibrium with a model melt of *c.* 6·3 wt % MgO, whereas its rim yields a model melt of *c.* 8·5 wt % MgO. Groundmass olivines in the MOZ and UOZ yield model melts of *c.* 8 wt % MgO.

Clinopyroxene

To calculate the MgO and FeO of the melt in equilibrium with clinopyroxene we used the clinopyroxene Fe/Mg ratio and a clinopyroxene–melt K_d calculated using equation (14) of Bédard (2010). Interstitial LBZ clinopyroxene yields evolved model melts of *c.* 5–3·5 wt % MgO. In the LOZ and MOZ, clinopyroxene oikocryst cores yield primitive model melts between *c.* 9 and 7 wt % MgO, as do euhedral cumulus clinopyroxene cores in the UOZ. All clinopyroxene rims in the OZ yield Fe-rich compositions with model melts $<$7 wt % MgO. The cores of cumulus clinopyroxenes from the CPZ yield compositions (*c.* 9–6 wt % MgO), similar to the range of model melts recorded by OZ clinopyroxene, whereas their evolved rims and interstitial clinopyroxene in the CPZ yield very evolved model melts with $<$5 wt % MgO. Model melts calculated from the DZ clinopyroxene cores show cryptic up-section variation with melt MgO broadly ranging between *c.* 8 and 1 wt %. In the UBZ, dendritic clinopyroxenes correspond to model melts ranging between *c.* 7 and 1 wt % MgO. A coarser, sector-zoned clinopyroxene in the UBZ yields model melts of *c.* 6·5 wt % MgO, with values of *c.* 2 wt % MgO in the sieve-textured mantle and more primitive melts of *c.* 5 wt % at its rims.

DISCUSSION

Constraints provided by the mineral-chemical data and inverse melt compositions

Olivine and clinopyroxene in the LPS yield a broad range of model melt MgO compositions. When coupled with the textural observations, these allow us to track the chemical evolution of melts within the LPS. The cores of euhedral olivine phenocrysts and primocrysts

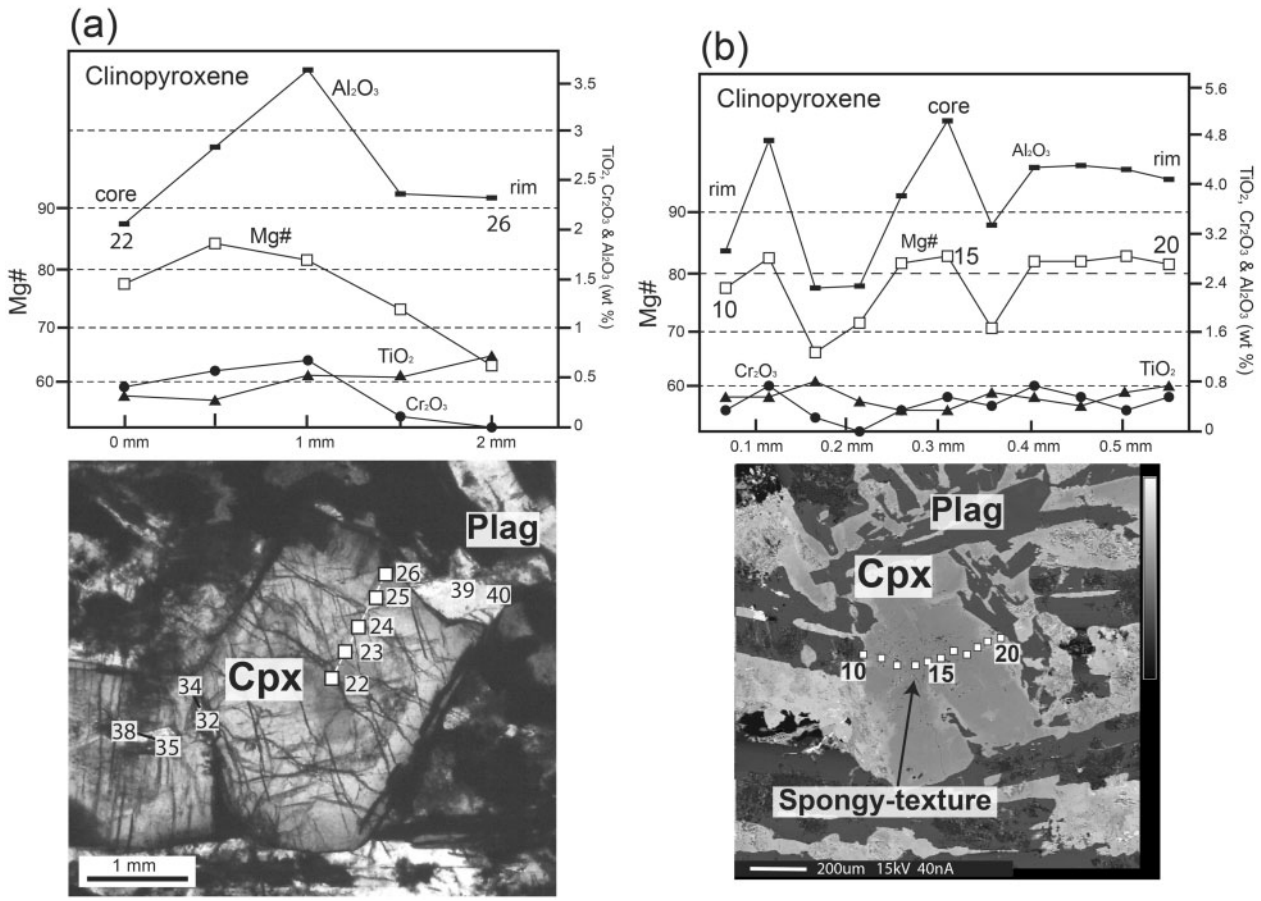

Fig. 14. (a) Plane-polarized light photomicrograph of a euhedral clinopyroxene crystal from the DZ, with the corresponding microprobe traverse (Nos 22–26). The clinopyroxene shows outward increase of Mg# and Cr_2O_3 in its mantle before developing normal zoning at its rim, suggesting that it may have equilibrated with a more primitive melt during crystallization. (b) BSE image of a clinopyroxene crystal from the UBZ that has a sieve-textured core–mantle. The microprobe traverse (Nos 10–20) shows complex zoning with a high-Mg# core followed by low-Mg# mantles and outwardly decreasing Mg# at the rims, a pattern that is mimicked by Al_2O_3.

within the LCM, LBZ and LOZ yield the most primitive model melt MgO compositions (*c.* 13·5–10 wt % MgO), equal to or higher than the MgO content of their host chills (10·3 wt %), but similar to the most primitive chilled margins from other Type-1 Franklin sills (Bédard *et al.*, 2013). The majority of olivine phenocryst rims from the LCM, as well as olivine phenocryst cores from the LBZ, are, however, in approximate equilibrium with the LCM composition. The model melt compositions in equilibrium with olivine chadacrysts included in clinopyroxene oikocrysts have MgO values between *c.* 10 and 8 wt %. The melt values calculated to be in equilibrium with the most primitive poikilitic clinopyroxene (*c.* 9–8 wt % MgO) fall within this range of melt compositions. Because these clinopyroxene oikocrysts contain both normally and reversely zoned olivines, the clinopyroxene oikocrysts in the OZ must have formed after some of their enclosed olivines were exposed to a higher-MgO melt.

The primitive melt values calculated from the cores of olivine and clinopyroxene are in stark contrast to the values for melts calculated from olivine cores in the UOZ. Melt values in equilibrium with UOZ olivine cores are as low as *c.* 5 wt % MgO, whereas the rims extend to melt values of *c.* 8 wt % MgO. These reversely zoned trends are seen in hopper olivines, groundmass olivines and rare primocrystic olivines in the UOZ. Reversely zoned primocrystic olivines contain Cr-spinels that mirror the Fo trend (Fig. 10). Cr-spinel hosted within the low-Fo olivine core has lower Cr# and higher Fe2# and Fe3# than the Cr-spinel hosted by the more primitive olivine rim. This pattern suggests that the Cr-spinel in the primocryst rim formed from a less evolved melt than the one in the core, as also implied by the host olivine primocryst zoning.

In addition to the common occurrence of reversely zoned olivines in the UOZ, groundmass olivines become more primitive upward in the OZ. In the LOZ, groundmass olivines typically have compositions of Fo_{75} (*c.* 5 wt % MgO model melt). This increases to Fo_{80} (*c.* 8 wt % MgO model melt) in the MOZ and UOZ. MOZ and UOZ groundmass olivines are therefore in equilibrium with the rims of reversely zoned UOZ olivines, suggesting that they may have crystallized from the same melt. The shift to more primitive groundmass olivine compositions upward through the OZ may indicate a change in the crystallization conditions or differing proportions of trapped melt in this region of the OZ.

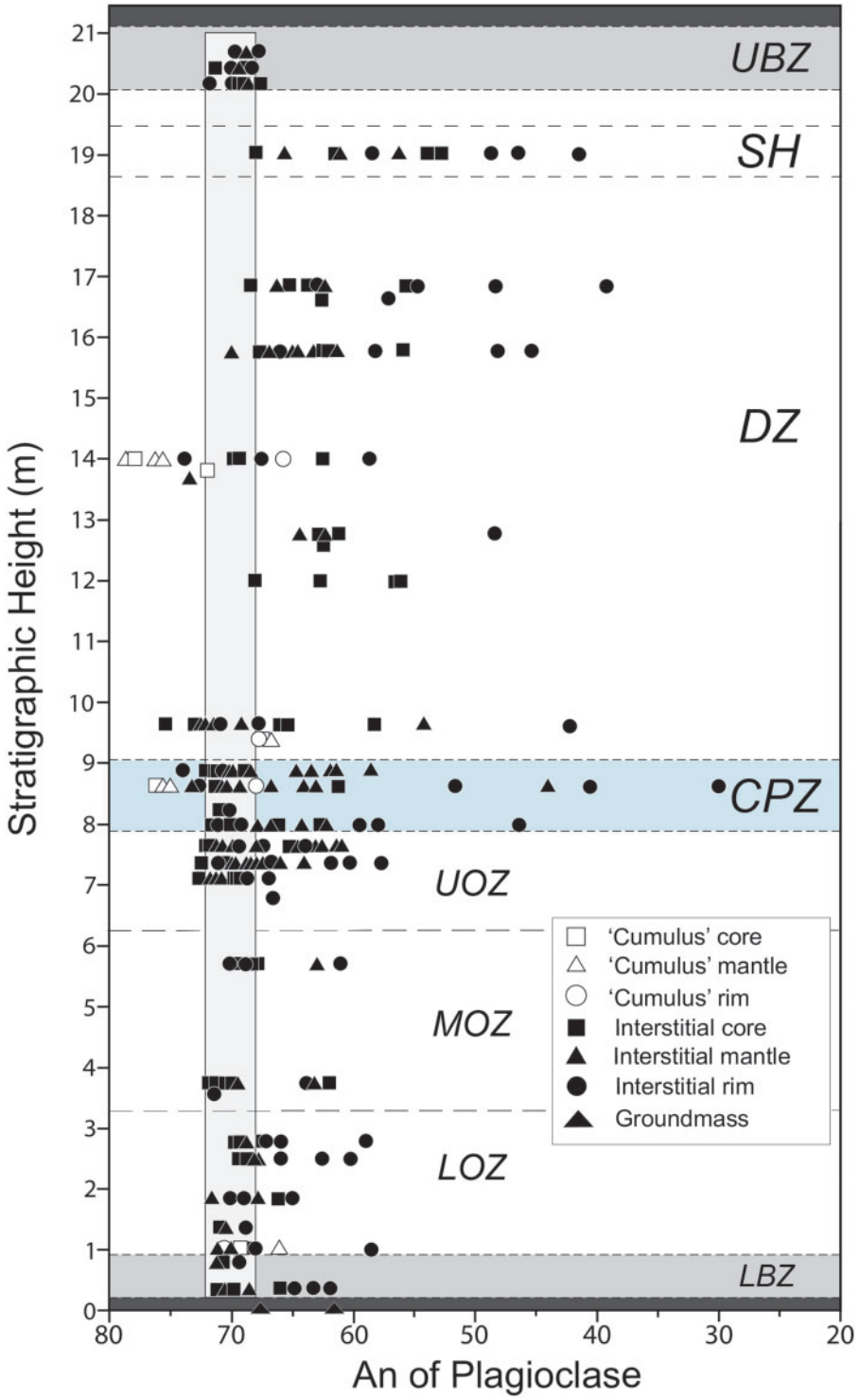

Fig. 15. Stratigraphic column showing plagioclase compositional variations in molar anorthite [An = 100Ca/(Ca + Na + K)] content through the LPS. The vertical grey rectangle indicates the typical range of core compositions throughout the LPS ($An_{72–68}$).

Recorded clinopyroxene model melt variations at the base of the DZ are in equilibrium with OZ clinopyroxenes (*c.* 9–7 wt % MgO), before becoming more evolved up-section to reach minimum MgO contents (*c.* <4 wt % MgO) in the upper DZ (sandwich horizon). Rims to euhedral clinopyroxenes in the DZ are in equilibrium with DZ interstitial clinopyroxenes (*c.* 4–1 wt %). Throughout the LPS, clinopyroxene rims locally record extreme Fe–Ti-enrichment, presumably as a result of extensive *in situ* differentiation of pore melts (see Humphreys, 2009). If the interstitial clinopyroxenes throughout the LPS crystallized from late, evolved pore melt then this implies that the larger clinopyroxenes may also have crystallized from or equilibrated with this melt. The

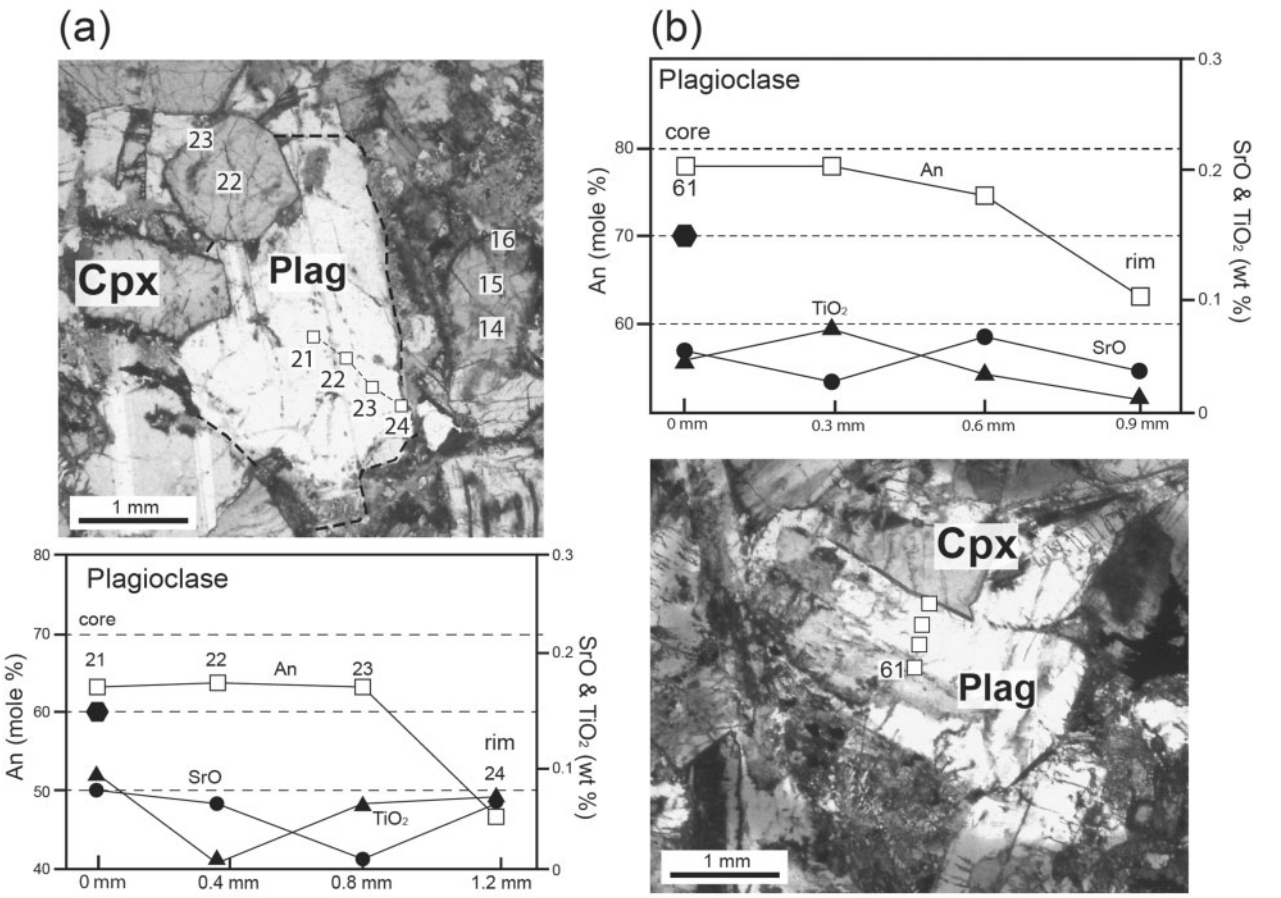

Fig. 16. (a) Plane-polarized light photomicrograph of an interstitial plagioclase crystal from the CPZ with the corresponding microprobe traverse (Nos 21–24). A *c.* 1 mm sized euhedral sector-zoned clinopyroxene can also be seen (Nos 22 and 23). The plagioclase is strongly normally zoned with An values of <50 mol % at the rims. (b) Plane-polarized light photomicrograph of a euhedral plagioclase lath (possibly cumulus?) in the DZ, with the corresponding microprobe traverse (No. 61). This plagioclase has the highest core An (An_{77}) content recorded in the LPS and is normally zoned towards its rim. Filled hexagon = average An content.

upward evolution in clinopyroxene rim compositions (eventually to values of Mg# *c.* 20: Fig. 11) is matched by shifts in the plagioclase rim–interstitial plagioclase compositions (*c.* An_{40}: Fig. 15) suggesting the presence of a sandwich horizon, possibly formed by migration and pooling of evolved pore melt (Boudreau & Philpotts, 2002) in the last part of the sill to solidify (i.e. the mid–upper DZ). A coarse UBZ clinopyroxene crystal yields a broader range of model melts (*c.* 7–4 wt % MgO) compared with dendrites in the LBZ (*c.* 4–3 wt % MgO) and may therefore be a 'xenocrystic' crystal that was carried in with the first pulse of LPS magma.

PELE modeling

To help constrain the crystallization history of the sill, we ran the PELE program (Boudreau, 1999) using the LPS chill (*c.* 10·3 wt % MgO) as a starting composition. A fractional crystallization model was run at a pressure of *c.* 0·8 kbar, corresponding to the estimated height of the overlying stratigraphic column. Melt CO_2 was set at 0·2 wt %, S at 0·12 wt % and H_2O at 0·2 wt %, and chromite was excluded from the assemblage (justifications are provided in the Supplementary Data electronic appendices). PELE predicts a liquidus at 1245°C where Fo_{88} olivine crystallizes, values similar to the core compositions of olivine phenocrysts in the LCM. After *c.* 8% olivine was extracted, PELE predicts that the melt co-saturates in clinopyroxene (Mg# 87) and plagioclase (An_{80}) at *c.* 7·5 wt % MgO (1175°C), at which juncture the composition of olivine is Fo_{84}. PELE predicts that olivine reaches compositions of Fo_{75} (similar to primocryst rims in the LOZ and the most evolved primocryst cores from the UOZ) at *c.* 1115°C, at which point the sill would be 40% solidified, comprising 11% olivine + 16% plagioclase + 13% clinopyroxene + 60% pore melt with an MgO content of 6 wt %. In conclusion, the crystallization pathway predicted by PELE is broadly compatible with the observed compositions and textures of olivine in the LPS OZ. However, the most primitive model melts calculated to be in equilibrium with clinopyroxene (*c.* 9 wt %) exceed the melt MgO composition at which clinopyroxene becomes co-saturated according to the PELE model (*c.* 7·5 wt %). Conversely, the model melts calculated to be in equilibrium with most DZ clinopyroxene are in accord with the PELE results. We now discuss the role that fractional crystallization may have played in the differentiation of the LPS.

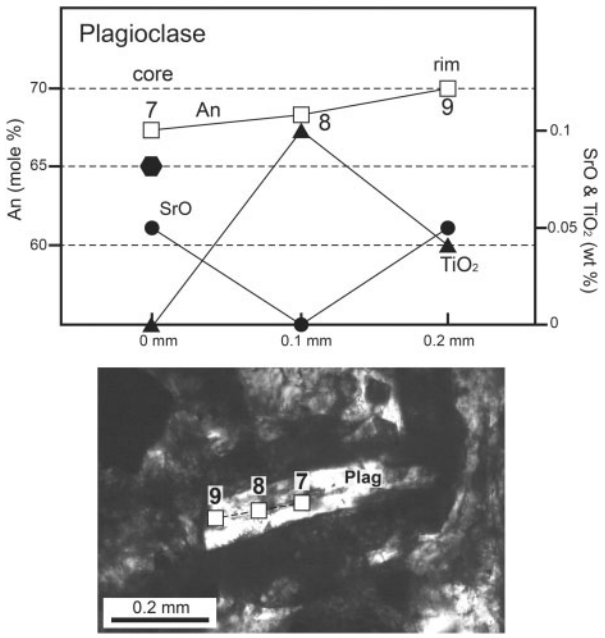

Fig. 17. Plane-polarized light photomicrograph and microprobe traverse (Nos 7–9) of a plagioclase crystal in the UBZ. This plagioclase is reversely zoned with increasing An towards its rim. Filled hexagon = average LBZ plagioclase composition.

The role of closed-system fractional crystallization in the LPS

Mineral compositional trends in a related suite of igneous rocks are commonly explained by fractional or equilibrium crystallization (Bowen, 1928). The classic example is the Skaergaard intrusion, which exhibits unambiguous mineralogical and cryptic mineral-chemical trends interpreted to reflect closed-system fractional crystallization of a single pulse of magma (Wager & Deer, 1939; McBirney, 1996; Tegner, 1997). In the LPS we see similar signs of compositional evolution that could be interpreted as being due to *in situ* fractional crystallization. Such an interpretation would imply that the sill was initially filled with an olivine + chromite-phyric magma; that all of the olivine settled out to yield the OZ and that after the olivine settled out co-saturation of clinopyroxene yielded the CPZ, followed almost immediately by plagioclase co-saturation and reaction of olivine to low-Ca pyroxene to produce the basal DZ. The diffuse inward trends seen in the DZ mineral chemistry of both clinopyroxene (Fig. 11) and plagioclase (Fig. 15) suggest that the DZ solidified mainly at the floor and reached its furthest chemical evolution in a sandwich horizon just below the UBZ. In such a model the systematic decrease in Fo from olivine primocrysts, to chadacrysts, to groundmass in a single thin section would record *in situ* evolution of trapped pore melt that partly reacted with its cumulate matrix. However, although many aspects of such a scenario are plausible, the petrology of the LPS suggests a more complex differentiation history.

None of the main mineral species within the OZ exhibits trends suggesting systematic up-section fractional crystallization by sequential crystallization against the floor (Figs 9, 11 and 15). Given the extreme compatibility of nickel in olivine (Arndt, 1977; Hart & Davis, 1978), nickel in accumulated olivine should show a marked and rapid up-section decrease, a pattern that is not observed in the LPS OZ. Alternatively, the uniform compositions of the various olivine morphologies in the LPZ OZ could be explained if these olivines remained in suspension and re-equilibrated with melt (equilibrium crystallization path) prior to deposition, as in the model proposed by Huppert & Sparks (1980) and Tait (1985). This scenario also fails to explain the observations, because in such a model the deposited olivines should be essentially unzoned, or at least show a consistent normal zoning pattern, whereas olivines in the LPS OZ show marked diversity of composition and zoning pattern. The common preservation of hopper olivine habits in the LPS OZ also seems inconsistent with this scenario, because hopper olivines would have recrystallized during settling to become more euhedral (Welsch *et al.*, 2012).

Nor are the modal abundances of olivine in the LPS compatible with the amounts of olivine predicted to crystallize from the magma by the PELE modeling. The olivine present in the OZ (when redistributed throughout the LPS) represents *c.* 15–20% of the volume of the LPS (assuming constant thickness). This is far in excess of the *c.* 8% olivine-only crystallization predicted by PELE. This suggests that the amount of olivine in the LPS OZ was not extracted by *in situ* crystallization of a magma similar to the LPS chill. PELE models with a starting composition corresponding to some of the most primitive Franklin chills (*c.* 13·5 wt % MgO) crystallize slightly more olivine (*c.* 10–15%) prior to co-saturation in plagioclase and clinopyroxene and provide better fits to the observed modal abundances of olivine in the LPS OZ. It might be possible to explain the observed olivine modal abundances if the LPS was filled with a more primitive magma (in comparison with the observed chilled margin composition), or if the initial melt pulse carried a significant cargo of olivine crystals (*c.* 20%). However, neither of these alternative models is compatible with the variety of olivine zoning patterns and their organized distribution within the OZ.

In conclusion, we contend that the common occurrence of reversely zoned olivines in the UOZ and the presence of evolved Cr-spinel inclusions in the low-Fo olivine cores of such grains (Fig. 10) cannot be explained by *in situ* fractional crystallization of a single melt pulse and require the operation of an additional mechanism during sill formation and differentiation.

The significance of reversely zoned olivine

The survival of strongly zoned olivine in the LPS, particularly the reversely zoned olivines, and the heterogeneous olivine compositions from single thin sections imply preservation as a result of rapid cooling. The presence of heterogeneous olivine compositions within single thin sections is reminiscent of the diversity of

olivine Fo compositions observed in Hawaiian picrites (Garcia *et al.*, 2003). Preliminary olivine Fe = Mg diffusion calculations following the method of Costa & Dungan (2005) suggest that the residence time of olivine at magmatic temperatures (with a closure temperature of *c.* 1150°C) was between *c.* 2 and 5 years. Following the method of Carslaw & Jaeger (1959) for 'simple' conductive heat loss of a sill to wallrock at 75°C, between 3 and 6 years are needed to cool magma to its solidus, similar to the time calculated above. Using a method similar to that described by Cawthorn & Walraven (1998) yields a very similar cooling rate. These calculations indicate that the LPS cooled rapidly and imply that opportunities for re-equilibration were limited. Consequently, we conclude that the mineral-chemical signatures recorded in the LPS are primary igneous features.

Reversely zoned olivines are present throughout the OZ but they are particularly common in the UOZ. In the LOZ, olivine chadacrysts enclosed by clinopyroxene preserve subtle reverse zoning, indicating reaction with primitive melts containing *c.* 10 wt % MgO. According to the PELE modeling such melts would be saturated only in olivine + chromite. One of the most extreme examples of a reversely zoned olivine in the UOZ has an evolved core (Fo_{77}) that formed from a low-MgO (*c.* 6 wt %) melt that would have been in equilibrium with an olivine + clinopyroxene + plagioclase assemblage. The core of this olivine also contains an evolved (low-Cr#, high-Fe3#, high Fe2#) Cr-spinel that must have formed from a melt that had a low Mg# and high concentrations of ferric iron. In contrast, the Fo_{80} rim of this reversely zoned olivine indicates formation from a more primitive melt with *c.* 8 wt % MgO, and it contains Cr-spinel inclusions with compositions (high Cr#, low Fe3#, low Fe2#) that also imply an outward shift to more primitive melt compositions. Reverse zoning (rimward Mg# and An increases) is also seen in both clinopyroxene and plagioclase (Figs 11 and 15) throughout the LPS. We hypothesize that these reverse mineral-chemical zoning trends in clinopyroxene and plagioclase may possibly be related to the same mechanism that produced the reversely zoned olivines in the OZ.

The different textural types of olivine and their distinct compositions, when considered together with the presence of reverse zoning (in both olivine + Cr-spinel inclusions) in the OZ, strongly suggest that the OZ rocks are hybrids, representing a mixture of multiple generations of crystallization products and liquids. Below, we attempt to constrain the different components involved in the differentiation of the LPS using the mineral and melt chemistry in combination with the PELE modeling results.

The origin of the OZ–DZ duality

The source of the high-MgO melts—an olivine slurry?

The presence of reversely zoned olivines in the OZ excludes an origin by simple fractional or equilibrium crystallization of a single pulse of melt. We propose that this reverse zonation is the result of an intra-sill melt replenishment event and that the primitive rims record the arrival of a replenishing magma into the LPS. The range of primitive melt compositions calculated from the reversely zoned rims of olivine in the OZ is between *c.* 10 and 8 wt % MgO. These melts resemble the LPS chilled margin composition and would have had about the same composition as the melts from which most of the primitive olivine primocrysts in the LOZ formed. Some of the olivine primocrysts are too primitive to have crystallized from a melt similar to the LPS chilled margin, however, and may be exotic to the LPS. The highest model melt MgO contents (up to *c.* 13·5 wt %) recorded in the OZ may represent the replenishing melt, but it is also possible that the high-Fo primocrysts that yielded these high melt MgO contents are unre-equilibrated antecrysts derived from a less-evolved magma that was actively fractionating olivine somewhere upstream as it flowed towards the LPS.

The melt–crystal systematics leads us to infer that a magma containing olivine primocrysts was emplaced into the LPS as a replenishing olivine slurry. In this scenario, the primitive carrier melt is responsible for the reverse zoning of OZ olivines, with the low-Fo cores of these grains being relicts of the crystal mush that was present in the sill before the slurry arrived. The late arrival of a crystal–liquid slurry carrying a cargo of primitive olivine primocrysts would account for the excess modal olivine in the LPS as a whole compared with the PELE fractional crystallization model. On the other hand, the diverse zoning patterns observed in the OZ, particularly the reverse zoning, appear inconsistent with models invoking simple redistribution of entrained olivine carried in by an initial magma. In this context, the low-Fo hopper olivines in the MOZ and UOZ might also reflect contamination of the primitive slurry by host DZ rocks. Radiogenic and $\delta^{34}S$ isotope data (Hayes *et al.*, in preparation) show that the OZ and DZ are not in isotopic equilibrium and represent separate intrusive events, strongly supporting a multiple intrusion model.

We propose that a slurry of olivine primocrysts was emplaced immediately above the dendritic LBZ (at *c.* 1 m above the lower contact) and beneath the DZ, to form the LPS OZ. We speculate that the boundary between the (solidified) dendritic LBZ and the relatively buoyant feldspar-rich resident mush above was an important mechanical discontinuity, facilitating emplacement of a slightly denser olivine slurry. The primitive melt in the replenishing magma would have partly mixed with the resident, evolved, gabbroic mush. Some of the evolved olivines in the OZ may be true relicts, whereas others may record more extensive, earlier hybridization steps. Because the primitive olivine primocrysts with normal zoning patterns typify the LOZ, we suggest that this sub-zone is the least-hybridized facies of the OZ and mostly contains olivines carried in by the replenishing slurry. Reversely zoned mantles to some olivine phenocrysts from the LBZ (Fig. 9), which we infer are derived from the first magma pulse emplaced

into the LPS, may also have developed as a result of olivine slurry emplacement, through heating and impregnation of a porous floor. However, reversely zoned mantles are also observed in LCM olivine phenocrysts, so we cannot rule out the possibility that the reversed zoning signatures were created further upstream in the plumbing system prior to emplacement in the LPS. It is also possible that the melt directly in contact with host dolostone may have increased its Mg/Fe by assimilating some of the wallrock dolostone (see Gaeta *et al.*, 2009; Di Rocco *et al.*, 2012; Hayes *et al.*, submitted).

Reversely zoned olivines and chromite microphenocrysts are observed in many of the olivine-cumulate sills in the Minto Inlier, suggesting that late olivine slurry emplacement may be common in Type-1 Franklin sills (Hayes *et al.*, in preparation).

The DZ—a relict of the resident mush?

Thin hypabyssal sills and dikes (such as the LPS) are typically considered to have been emplaced near instantaneously and to have cooled rapidly. As a result they should show limited internal differentiation. They commonly have doleritic textures, which would have hindered crystal–liquid separation, so giving them only a weak cumulate component (Gunn, 1966; Philpotts *et al.*, 1998). The compositions of model melts in equilibrium with DZ clinopyroxene cores are typical of cotectic melt compositions (*c.* 7·5 wt % MgO). The compositions, textures, scarcity of cumulus minerals (<10%) and abundance of Fe–Ti oxides of the LPS DZ are therefore typical of relatively quickly crystallized hypabyssal sills.

If the evolved cores of reversely zoned olivines in the UOZ are relicts of the earlier gabbroic material filling the LPS, as argued above, then we can use their composition to constrain the DZ composition prior to replenishment. The most evolved olivine core (*c.* Fo_{75}) in the UOZ that has a reversely zoned rim is in equilibrium with a model melt composition of *c.* 6 wt % MgO. The PELE and Fe = Mg modeling indicate that plagioclase and clinopyroxene joined olivine on the DZ liquidus at *c.* 7·5 wt % MgO. This implies that the low-Fo (Fo_{75}) cores in the OZ should have been part of a three-phase cotectic gabbroic assemblage. If the DZ crystallized from a melt similar to the LPS LCM, then the PELE modeling suggests that at the moment when the replenishing event occurred, the DZ would have comprised 11% olivine, 16% plagioclase, and 13% clinopyroxene with 60% pore melt. Henceforth we refer to this assemblage as the resident mush.

One disparity between this model and the observations is that no olivine has been observed in the DZ, whereas PELE predicts *c.* 10% to have been present in the pre-replenishment LPS. There is commonly a thin olivine-gabbro subzone at the base of the DZ in other Franklin sills of this type (e.g. Bédard *et al.*, 2012), so we infer that the sparse (*c.* 5–10%) orthopyroxene from the basal LPS DZ may be pseudomorphous after olivine. This implies that the interstitial melt in the LPS DZ became sufficiently evolved to have reached the olivine–orthopyroxene peritectic, which is consistent with the highly evolved compositions of crystal rims in the DZ (e.g. clinopyroxene Mg# 20; Fig. 11).

The primitive plagioclase (An_{77}) and clinopyroxene (Mg# 85) crystals in the DZ that are now embedded in a mass of later *in situ* crystallization products may be relicts of early DZ crystallization, antecrystic phases that were carried into the LPS by the first pulse of magma, or grains entrained from a syn-replenishment hybridization zone into the DZ above. Reversely zoned mantles in cumulus-textured clinopyroxene in the CPZ and DZ, and localized reverse zoning in cumulus plagioclase in the DZ, may record the arrival of the OZ replenishing magma, but this remains conjectural.

Following olivine slurry emplacement, we suggest that the DZ continued to evolve, reaching its most extreme mineral compositions (Figs 11 and 15) and highest proportions of accessory phases (Fe–Ti oxides, amphibole, biotite) at a high-level sandwich horizon, a pattern suggestive of progressive *in situ* fractional crystallization (see Boudreau & Philpotts, 2002). Although we cannot unequivocally determine whether the DZ sandwich horizon developed prior to or after olivine slurry emplacement, we will argue below that it postdates it.

Mixing and hybridization between the resident DZ and replenishing magma

We propose that a partly crystalline DZ (*c.* 40% solid) was resident in the LPS when a replenishing olivine-charged magma was emplaced. The replenishing magma must have contained a high melt fraction (*c.* 50%) as otherwise flow would have been impeded (Paterson, 2009). We further propose that mixing between the slurry and resident magma led to the formation of a hybrid melt with a composition of *c.* 10–8 wt % MgO, and we infer that the most primitive reversely zoned olivine rims and overgrowing clinopyroxene oikocrysts crystallized from this hybrid melt.

Clinopyroxene oikocryst cores have similar Mg# throughout the OZ, indicating that they all formed from melts with *c.* 9–8 wt % MgO. Conversely, the rims of reversely zoned olivines become less forsteritic upsection, from Fo_{83} in the LOZ to Fo_{80} in the UOZ, where olivine rims are calculated to have been in equilibrium with *c.* 8 wt % MgO melts. The lack of differentiation in OZ clinopyroxene core compositions suggests that clinopyroxene co-saturated when the local pore melt reached the same point in its compositional evolution. The model melts calculated to be in equilibrium with OZ clinopyroxene exceed their cotectic melt MgO content (according to PELE), suggesting that these clinopyroxenes did not form through fractional crystallization from the LPS LCM melt composition. Instead, OZ clinopyroxene saturation appears to have been triggered by magma hybridization at *c.* 9 wt % MgO.

The compositions of groundmass olivines in the MOZ are more primitive than LOZ groundmass olivines

and are in equilibrium with reversely zoned rims in the UOZ. The transition to more primitive groundmass olivine in the MOZ–UOZ suggests that these groundmass olivines crystallized from hybrid magma percolating up through this mass as the OZ cumulates became compacted. As such, the UOZ rim compositions were buffered by throughflow from hybrid pore melt expelled from below. However, compaction of the OZ may have been limited by the relatively rapid cooling rate of the LPS (<6 years). We suggest that the UOZ is a strongly hybridized facies of the OZ that retains undissolved traces of the resident mush, now represented by plagioclase and clinopyroxene inclusions in hopper olivines (Fig. 5d and f), evolved olivine cores and evolved Cr-spinel inclusions (Fig. 10). The less common MOZ hopper olivines (Fig. 5b) may also have crystallized from hybrid magma, possibly suggesting a weaker contamination signature in the MOZ.

Evidence for rapid crystallization in the center of the LPS

Hopper olivine morphologies in the UOZ

The UOZ is characterized by abundant hopper olivine morphologies (Fig. 5d–f), some of which are reversely zoned. The hopper olivines of the UOZ that enclose clinopyroxene and plagioclase (Fig. 5d and f) are also inferred to record ingestion of the DZ mush by the olivine slurry. Experiments carried out by Donaldson (1976) show that olivine crystal morphology is related to the cooling rate and melt MgO composition, and that hopper olivine morphologies form at high growth rates. Huppert & Sparks (1980) suggested that hopper and elongate olivines could be produced by rapid cooling when a hot, primitive basaltic magma quenches beneath a cooler basaltic melt. A very similar mechanism was proposed more recently for the origin of cyclic harristic layering in the Rum intrusion (O'Driscoll *et al.*, 2007). The hopper olivines in the UOZ of the LPS seem to indicate rapid cooling, even though the UOZ is near the middle of the LPS (at *c.* 8 m height) where cooling rates should be the slowest. We suggest that the hopper olivine in the LPS OZ formed when the hotter, primitive olivine slurry intruded a cooler resident gabbroic mush. In this scenario, the 'supercooled' hybrid melt crystallized olivine (hopper-type) around the xenocrystic cores sourced from the resident gabbroic mush.

Sector-zoned clinopyroxene in the CPZ

Above the OZ there is a striking modal and textural change as olivine cumulates grade rapidly into a thin layer dominated by euhedral, sector-zoned clinopyroxene (Fig. 7). The passage from olivine-dominated cumulates to a clinopyroxene-rich cumulate assemblage (CPZ) could be interpreted as being due to fractional crystallization with co-saturation in clinopyroxene briefly preceding co-saturation with plagioclase. However, as discussed above, our preferred interpretation is that the OZ formed as a replenishment into a

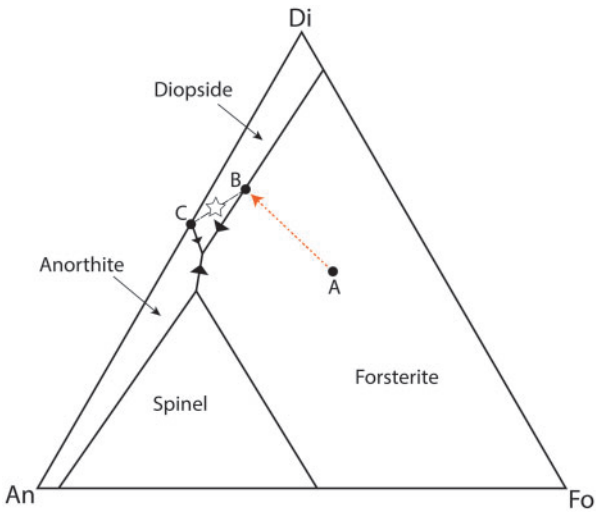

Fig. 18. Di–An–Fo phase diagram modified after Onuma & Tohara (1983) and Bédard (1993), indicating how a mixture of a melt that has crystallized on a path from the olivine (Fo) phase field (A) to the clinopyroxene (Di) cotectic (B), with a melt that has crystallized plagioclase (C), falls in the clinopyroxene-only field (labeled with a star). Melt A would originally be olivine slurry-derived carrier melt that became hybridized and crystallized olivine and clinopyroxene (Melt B). Melt C would be derived from the DZ, which had crystallized plagioclase. Melt C was most probably late Fe-enriched pore melt that percolated down through the DZ mush.

resident gabbroic mush (DZ). This suggests that the CPZ may be related to this event, rather than representing an intermediate fractional crystallization step.

The development of sector-zoning in clinopyroxene has been attributed to rapid growth brought about by rapid cooling, or quenching by magma decompression and volatile exsolution (Nakamura, 1973; Brophy *et al.*, 1999). However, as emphasized in the discussion about the origin of hopper olivines, the CPZ is roughly in the middle of the sill (at *c.* 8–9 m height), where cooling rates should be slowest. Also, clinopyroxene was not a liquidus phase upon emplacement of the initial LPS melt (assumed to have had a composition corresponding to the LCM), so decompression and volatile exsolution are not plausible causes. In the context of the OZ emplacement model we suggest that the rapid growth textures and abundant clinopyroxene modes of the CPZ record compositional super-saturation induced by pore-scale melt mixing. If the DZ was underplated by an olivine slurry, then the OZ–DZ interface may have been overprinted by the migration of pore melts from one system into the other. We speculate that the buoyant, hybrid melts from the OZ percolated upwards, possibly driven by compaction of the OZ below, and infiltrated the base of the DZ, where pore melts would have had cotectic compositions. The phase topology (Fig. 18) suggests that mixtures of two such melts could result in a clinopyroxene-only saturated melt (Onuma & Tohara, 1983; Bédard, 1993). Clinopyroxenes that form from such compositionally super-saturated melts may have crystallized rapidly, much as we suggested for the hopper olivine of the UOZ. This interpretation for the origin

of the CPZ is consistent with the distribution of sector-zoned clinopyroxene into 'channel-like' trains (Fig. 8). It is also supported by the compositions of the sector-zoned clinopyroxene, which have core compositions (Mg# 85–83) that overlap with core compositions of clinopyroxene oikocrysts in the OZ below (Fig. 11). Because the latter are interpreted to have crystallized from the hybrid melt of the OZ, this compositional similarity is consistent with derivation of the sector-zoned clinopyroxene from pore melt expelled from the OZ.

Model—the development of igneous layering in the LPS

Based on the textural and mineral-chemical evidence presented above, we propose that the LPS records three main magmatic stages (Fig. 19): (1) initial magma (a dilute crystal slurry) emplacement followed by fractional crystallization; (2) replenishment and partial hybridization with an olivine slurry; (3) late-stage pore melt migration, and limited re-equilibration with cooling, trapped pore melt.

Stage 1—initial magma emplacement and fractional crystallization

The presence of *c.* 5% modal olivine phenocrysts (*c.* 1–2 mm) in the LPS chills suggests that the initial magma pulse probably carried small amounts of olivine, although we cannot exclude the possibility that higher proportions of olivine were concentrated in the center of the flow (Bhattacharji, 1967; Simkin, 1967). It is also possible that the initial magma carried a cargo of clinopyroxene and plagioclase, as evidenced by the presence of rare cumulus crystals in the DZ. Model melts in equilibrium with the most primitive olivine phenocrysts in the LCM have higher MgO contents (at *c.* 13 wt % MgO) than the LPS chill (10·3 wt % MgO). As such, some of the olivine carried in with the first pulse may be antecrystic relicts (or products of an earlier crystallization step) carried downstream as the magma fractionated. After emplacement, this basaltic magma crystallized from both margins, producing the LBZ and UBZ, where high cooling rates formed plagioclase and clinopyroxene with dendritic habits that overgrew and cemented olivine phenocrysts. The olivine phenocrysts of the LBZ have core compositions that are in equilibrium with the LCM melt composition, suggesting that they are derived from this magma. The lack of any olivine crystals in the UBZ suggests that any phenocrysts that were present settled fast enough to evade entrapment by the downward solidification front.

The intergrowth of olivine with clinopyroxene and plagioclase dendrites in the LBZ suggests that the initial magma rapidly reached the three-phase cotectic after emplacement. If the LCM accurately reflects the melt composition, then only *c.* 8% olivine extraction is needed to reach three-phase saturation according to the PELE model. However, if the olivine phenocrysts in the chill are 'cumulate' phases, then the LCM composition is slightly biased towards higher MgO contents and <8% crystallization may be needed to reach three-phase saturation. If we deduct the average olivine core composition of LBZ olivines from the LCM (considering a 10% olivine mode for the LBZ), then the residual melt would contain *c.* 6 wt % MgO, similar to our estimate of the resident mush composition using the Fe = Mg modeling. The olivine that crystallized from this initial magma pulse into the LPS may have settled to form a first-stage olivine cumulate, but this cannot be determined with certainty. If such a basal olivine-rich layer developed at this stage then there may have been a weak S-shaped profile with the most evolved material concentrated in the upper third of the sill, as seen in other intrusions (Shirley, 1985; Meurer & Boudreau, 1998) and in thick lava flows (Bédard, 1987; Boudreau & Philpotts, 2002). The sandwich horizon defined by the clinopyroxene and plagioclase data from the LPS (Figs 11 and 15) may have developed early, or might have developed after emplacement of the olivine slurry (see below).

Stage 2—the emplacement of an olivine slurry and hybridization with the basal DZ

The mineral zonation patterns and compositions from the LPS OZ suggest that a crystal-charged olivine slurry was injected near the base of the LPS, beneath most of the buoyant DZ and above the more consolidated, dendritic-textured LBZ. This dynamic slurry could have scoured out and mixed with weakly consolidated (olivine-enriched?) host material resting on the sill floor, with only the better-consolidated, largely solidified LBZ adjacent to the cooling surface surviving. The relative coarseness of the LBZ dendrites (Fig. 3b) suggests relatively slow cooling rates, possibly owing to the emplacement of the hot olivine slurry above. If this is correct, it would imply that the olivine slurry arrived not long after the initial magma was emplaced into the LPS.

The olivine slurry would have been denser than a partly solidified, feldspar-rich dolerite, and so it would probably have underplated the host DZ, much as was proposed previously for the replenishment of magma chambers (Huppert & Sparks, 1980; Tegner *et al.*, 1993). On the basis of major element geochemical systematics, Hayes *et al.* (in preparation) calculated that the olivine slurry contained *c.* 20–25% olivine, making it slightly denser than a resident mush that was *c.* 40% solidified. Also, the 40% solidified resident mush may have been mechanically strong owing to formation of feldspar chains (Philpotts *et al.*, 1998), and so the weakest part of the LPS may have been the interface between the dendritic LBZ and the overlying partly crystalline resident mush. We infer that the emplacement of the olivine slurry at the base of the LPS created the S-type basal MgO bulge (Fig. 2b). During emplacement, we suggest that the incoming olivine slurry mixed to some extent with the resident mush (corresponding to the missing basal DZ) and created a hybrid melt with *c.* 10–8 wt % MgO. The evolved olivine cores (and evolved Cr-spinel inclusions) and possibly the gabbroic inclusions in hopper olivines

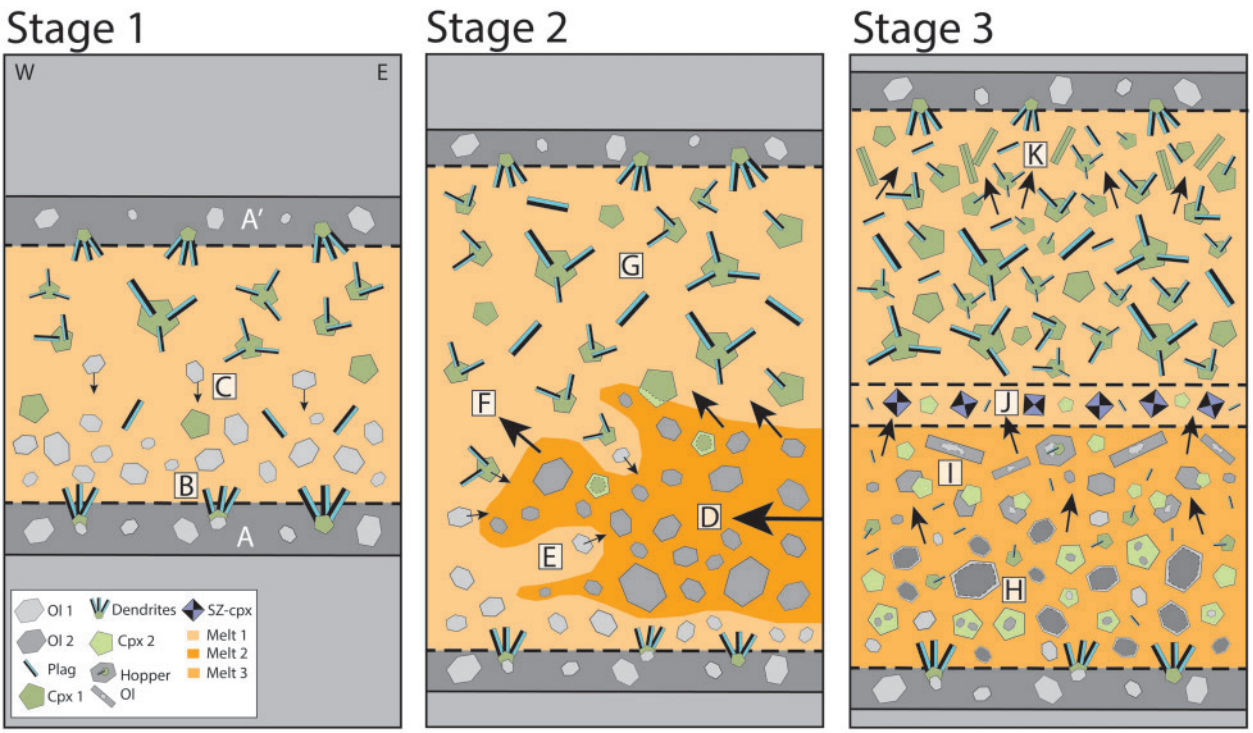

Fig. 19. Schematic illustrations showing the differentiation and subsequent formation of the OZ–DZ duality within the LPS. Stage 1 depicts the emplacement of the first magma in the sill. The initial magma was olivine + chromite phyric (Ol 1). Evidence of this early cargo of normally zoned olivine phenocrysts was quenched in, in both lower (A) and upper (A′) chilled margins. As the melt cooled from its lower and upper margins, it crystallized plagioclase and clinopyroxene dendrites that cemented LBZ olivine phenocrysts (B). No olivine phenocrysts were preserved in the dendritic UBZ owing to rapid olivine settling. The magma continued to solidify, crystallizing olivine (Fo_{75}) + clinopyroxene (Cpx 1) + plagioclase (Plag), and contained *c.* 60% pore melt with 6 wt % MgO (Melt 1) (C). In stage 2, an olivine-charged replenishment arrived from the east (D), carrying primitive olivine primocrysts ($Fo_{88–82}$; Ol 2) in a primitive carrier melt (13–10 wt % MgO; Melt 2). As the olivine slurry was emplaced it partly mixed with and ingested the resident gabbroic mush in the sill (E). The buoyant resident gabbroic mush would have been underplated by the denser olivine slurry (F). After the olivine slurry under- or intraplated the resident mush, the DZ continued to crystallize (G). During stage 3, the majority of the primitive olivine primocrysts delivered into the sill settled to form a LOZ (H). The replenishing and host magmas hybridize (Melt 3), form abundant hopper olivines, and react with primocrysts and xenocrysts to generate reversed zoning (I). Poikilitic clinopyroxene (Cpx 2) in the MOZ forms from the hybrid melt as it percolates through the OZ. The hybridized melt in the OZ encounters Fe-rich residual liquids in the DZ, generating sector-zoned clinopyroxene (SZ-cpx; J). The DZ continued to crystallize, with evolved clinopyroxene and plagioclase rims in the upper DZ representing a sandwich horizon where late-stage, evolved pore melt may have pooled (K).

are interpreted to be partially digested relicts of this basal DZ. The high-An cumulus plagioclase and high-Mg# cumulus clinopyroxene in the DZ may be remnants of the primitive base of the DZ, much of which may have mixed with and dissolved into the feldspar- and pyroxene-undersaturated olivine slurry. However, the DZ may have had a complex history prior to OZ emplacement, so we cannot exclude the possibility that the uncommon primitive plagioclase and clinopyroxene from the DZ are unrelated to OZ formation. Olivines in the MOZ and especially the UOZ commonly have hopper-type morphologies (Fig. 5b–f). These may record the chilling effect of extensive hybridization, coupled with heat loss to the cooler DZ host, similar to models for the harristic layering of the Rum intrusion (Huppert & Sparks, 1980; O'Driscoll *et al.*, 2007).

Stage 3—late-stage processes

After emplacement of the olivine slurry and hybridization with the basal DZ host the hybrid melt in the resulting OZ had a composition of *c.* 10–8 wt % MgO. This range may represent heterogeneities in the amount of admixed DZ material. Alternatively, the variability of the MgO content may reflect post-hybridization fractional crystallization of the hybrid melt as the OZ solidified. During this consolidation and cooling phase, interstitial and poikilitic clinopyroxene and then plagioclase, began to form. The cores of the most primitive clinopyroxenes that envelop the reverse-zoned olivines are in equilibrium with a maximum melt MgO content of *c.* 9 wt %, recording clinopyroxene co-saturation from the hybrid melt. We do not yet have a clear explanation for why clinopyroxene appears earlier on the OZ crystallization path in comparison with the PELE model results.

It is plausible to infer that pore melt from the OZ was expelled by compaction to mix with the overlying DZ, and we suggest that this is the origin of the sector-zoned clinopyroxene in the CPZ. At this juncture, the melt being expelled from the OZ would have had

Table 1. Representative olivine compositions

Type	Region	SiO_2	TiO_2	Al_2O_3	Cr_2O_3	FeO	MnO	MgO	CaO	NiO	Total	Fo
LCM												
Phenocryst (166A1)	Core	40·9	0·0	0·08	0·08	12·1	0·17	47·4	0·28	0·33	101·4	87·4
	Mantle	40·5	0·0	0·08	0·04	11·8	0·14	47	0·28	0·37	100·3	87·7
	Rim	39·9	0	0·06	0·05	16·2	0·19	43·9	0·27	0·34	100·9	82·8
Phenocryst (166A1)	Core	39·8	0	0·04	0·06	13·6	0·17	46	0·24	0·28	100·2	85·8
	Rim	37·8	0·01	0·03	0·02	22·7	0·28	38·9	0·21	0·24	100·2	75·4
LBZ												
Phenocryst (166A2)	Core	38·6	0	0·4	0·5	13·8	0·12	44·7	1·15	0·32	99·7	85·2
	Mantle	39·3	0	0·04	0·06	13·3	0·2	46·5	0·26	0·3	99·9	86·2
	Rim	36·9	0	0·03	0·02	25·2	0·23	35·9	0·24	0·26	98·8	71·7
Groundmass (166A3)	Core	37	0	0·06	0·01	22·9	0·24	38·2	0·28	0·23	98·9	74·8
	Rim	36·8	0·03	0	0·02	24·6	0·35	36·3	0·2	0·18	98·4	72·5
LOZ												
Chadacryst (166A4)	Core	39·7	0	0·05	0·04	16·8	0·32	43·5	0·21	0·2	100·9	82·2
	Rim	39·7	0	0·03	0·05	16·1	0·14	44·1	0·21	0·24	100·6	83
Primocryst (166A5)	Core	39·8	0	0·06	0·04	11·5	0·19	47·7	0·3	0·38	99·9	88·1
	Mantle	38·9	0·01	0·05	0·05	14·3	0·25	45·5	0·27	0·32	99·7	85
	Rim	37·6	0	0·03	0·01	19·9	0·33	40·9	0·21	0·21	99·2	78·6
Groundmass (166A5)	Core	38·3	0	0·05	0·02	21·4	0·32	39·2	0·28	0·22	99·8	76·5
	Rim	38·3	0·01	0·05	0·05	21·1	0·31	39·6	0·21	0·18	99·8	77
MOZ												
Hopper (167A2)	Core	38·6	0	0·04	0·06	17·2	0·23	42·7	0·29	0·23	99·4	81·6
	Rim	39·1	0	0·03	0	20	0·31	41	0·2	0·25	101	78·5
Groundmass (167A2)	Core	38·4	0	0·04	0·03	16·4	0·16	43·3	0·26	0·26	98·9	82·5
	Rim	38·9	0	0·04	0·01	16·3	0·17	42·9	0·22	0·28	98·7	82·4
Chadacryst (167A3)	Core	38·9	0	0·05	0·04	17·3	0·23	43·5	0·23	0·25	100·5	81·7
	Rim	38·3	0	0·03	0·03	17·9	0·24	42·7	0·23	0·24	99·6	81
UOZ												
Groundmass (167A4)	Core	37·2	0·01	0·03	0·03	22·7	0·42	38·6	0·22	0·2	99·4	75·2
	Rim	38·1	0·01	0·04	0·04	19·9	0·3	41·3	0·28	0·28	100·2	78·8
Hopper (311B3)	Core	39	0·02	0·03	0·03	20·8	0·3	40·6	0·25	0·2	101·2	77·6
	Rim	39·2	0	1·01	0·02	18·9	0·27	41·3	0·24	0·22	101·3	79·5
Primocryst (311B3)	Core	38·7	0	0·04	0·05	19·6	0·31	41·1	0·25	0·2	101·2	77·5
	Mantle	39·4	0	0·03	0·01	19·4	0·24	41·6	0·26	0·19	101·1	78·9
	Rim	39·6	0·01	0·02	0·02	18·8	0·21	41·6	0·17	0·23	100·6	79·7

Table 2. Representative Cr-spinel compositions

Type	SiO_2	TiO_2	Al_2O_3	Cr_2O_3	Fe_2O_3	MgO	FeO	NiO	Na_2O	Total	Cr#	Fe2#	Fe3#
LCM													
Inclusion in olivine	0·09	0·69	19·9	41·4	7·87	8·78	21·7	0·09	0·02	101	58	58	9·5
(166A1)	0·1	0·37	25·9	38·5	6·7	14·2	13·9	0·25	0·02	100	50	35	7·6
	0·09	0·39	25·9	38·2	6·6	13·6	15	0·24	0·02	100	50	38	7·6
	0·07	0·76	23·7	37·9	9·4	13	15·7	0·29	0	101	52	40	10·9
LBZ													
Inclusion in olivine	0·2	2	10·9	28·7	25·9	4	0·06	0·1	0·01	98·5	64	78	35·4
(166A3)	4·4	1·7	10·9	27·7	28·9	12	15·2	0·2	0·02	101	63	42	38·4
LOZ													
Inclusion in olivine	0·07	1·5	20·5	33	14·3	8·8	21	0·2	0	99·7	52	57	18
(166A4)	0·08	0·5	21	36·6	10·2	8·7	20·9	0·2	0·02	98·7	54	57	13
	0·07	0·5	21·7	38·1	8·8	9·7	19·8	0·21	0·03	99·2	54	53	10·7
(166A5)	0·05	7·5	5·1	21·5	34·4	3·7	25·7	0·18	0	98·3	73	80	52·9
	0·07	1·9	10	41·4	15·5	5·3	24·8	0·05	0·04	99·2	74	72	20·8
MOZ													
Inclusion in olivine	0·05	0·39	11·1	35·5	20·3	5·16	24·4	0·18	0·01	97·4	68	73	27·1
(167A3)	0·7	5·6	3·67	20·1	37·4	3·15	25·9	0·22	0·03	97	79	82	58
UOZ													
Inclusion in olivine core (311B3)	0·03	9·2	4·23	13	41	3·17	28·7	0·22	0	100·7	67	84	67
In olivine rim	0·03	8·5	4·7	17·1	36·8	4	28·1	0·2	0	101·3	71	80	59·1
Inclusion in cpx	0·05	0·97	18	40·8	4·5	10·6	22·6	0·12	0·02	100·6	60	54	6
(311B4)	0·46	1·27	17	39·1	6·6	10·5	22·6	0·11	0·04	101·4	0	55	8·9

compositions roughly corresponding to the compositions of the reversely zoned olivine rims and clinopyroxene in the UOZ (*c.* 8 wt % MgO). When it penetrated the overlying DZ, this OZ-derived pore melt would have mixed with more evolved pore melts, possibly triggering rapid growth of sector-zoned clinopyroxene (Fig. 7). We suspect that mixing occurred in dissolution channels in what is now the CPZ and that clinopyroxene

Table 3. Representative clinopyroxene compositions

Type	Region	SiO_2	Al_2O_3	FeO	TiO_2	Cr_2O_3	MgO	MnO	CaO	Na_2O	Total	Mg#
LBZ												
Poikilitic (166A3)	Core	49·9	4·6	6	0·6	0·8	16·7	0·1	20·4	0·2	99·3	83·2
	Mantle	50·7	4	5·6	0·5	0·6	16·8	0·1	20·9	0·2	99·5	84·2
	Rim	50·4	3	7·1	0·4	0·3	16·8	0·2	19·3	0·2	97·8	80·8
LOZ												
Poikilitic (166A4)	Core	52·6	2·5	6	0·2	0·5	18·7	0·2	19	0·2	99·9	84·7
	Mantle	51·5	2·6	6·4	0·5	0·6	17·6	0·2	19·7	0·2	99·2	83·1
	Rim	50·2	2·9	9	1·1	0	15·6	0·2	20·1	0·3	99·4	75·5
Poikilitic (167A1)	Core	51	3·8	6·2	0·4	1	17·9	0·2	18·6	0·2	99·3	83·7
	Mantle	51·3	3·7	5·4	0·4	0·9	17·3	0·1	19·8	0·2	99	85·1
	Rim	51·6	3·4	6·8	0·6	0·6	17·2	0·2	19·2	0·2	99·8	81·8
MOZ												
Poikilitic (167A2)	Core	51·1	2·4	5·4	0·5	0·7	18·1	0·1	20·5	0·2	99	85·7
	Mantle	51·8	2·5	5·2	0·3	0·7	17·7	0·1	20·3	0·2	98·7	85·8
	Rim	51·7	3·1	6·7	0·6	0·6	17·5	0·1	19·5	0·2	100·2	82·3
Poikilitic (167A3)	Core	51	4·3	5·6	0·4	1·2	17·2	0·1	19·8	0·2	99·8	84·5
	Mantle	53·1	2·4	5·5	0·4	0·7	18·5	0·2	19·4	0·2	100·3	85·7
	Rim	52·2	2·4	7·6	1·2	0·4	17·6	0·2	18·8	0·2	100·7	80·5
UOZ												
Euhedral (167A4)	Core	51·6	3·3	5·6	0·3	1·2	17·5	0·1	20·1	0·3	100·1	84·8
	Mantle	52·3	2·5	6·2	0·3	0·7	17·9	0·2	19·3	0·2	99·6	83·7
	Rim	51·9	2·5	8·9	0·9	0·1	16·8	0·2	18·6	0·3	100·3	77·1
Interstitial (311B3)	Core	50	3·1	9·1	1·5	0·2	16·5	0·2	19	0·3	99·9	76·3
	Rim	50·9	2·5	8·1	1·1	0·2	16·4	0·2	19·8	0·3	99·7	78·2
Euhedral (311B3)	Core	51·6	3·5	5·8	0·5	0·9	16·3	0·2	21·1	0·3	100·4	83·4
	Mantle	52·7	2·3	6·3	0·4	0·6	18·2	0·2	19·4	0·2	100·2	83·8
	Rim	52·7	2·1	6·8	0·26	0·6	18·4	0·2	19·4	0·2	100·8	82·7
CPZ												
Sector-zoned (311B4)	Core	53·5	2	5·8	0·2	0·8	19	0·1	18·8	0·2	100·6	85·3
	Rim	51·5	2·1	13·8	0·75	0·04	14·4	0·4	17·7	0·25	100·9	65
Euhedral (167A5)	Core	51·1	2·1	7·2	0·2	0·4	17·8	0·2	19·2	0·2	98·3	81·5
	Mantle	50·6	2·1	8·4	0·3	0·1	17·7	0·2	18·6	0·2	98·2	79
	Rim	47·5	1·8	17·8	1	0·1	13·4	0·4	16·3	0·2	98·5	57·3
DZ												
Euhedral (167A8)	Core	52	2·1	5·8	0·3	0·3	18	0·2	19·9	0·2	98·7	84·7
	Rim	51·9	2·7	8·5	0·5	0·1	17·2	0·2	18·2	0·2	99·6	78·3
Subhedral (167A10)	Core	50·6	1·7	14·5	0.	0	14·6	0·3	16·8	0·2	99·4	64·2
	Mantle	50	2·3	14·1	0·8	0	14	0·3	17·2	0·2	99	63·9
	Rim	50·2	1·7	16·7	0·6	0	11·8	0·4	18	0·2	99·7	55·7
Bladed (167A11)	Core	50·7	2·8	11·6	0·6	0	16·2	0·2	18·6	0·2	100·9	71·3
	Mantle	50·1	3	13·5	0·7	0	15·7	0·3	17·3	0·3	100·7	67·5
	Rim	49·1	1·7	22	0·5	0·1	13·9	0·5	13	0·2	100·9	53

formed by this reaction overgrew and replaced the olivine-bearing gabbroic matrix of the CPZ (Fig. 8).

When permeability dropped to the point at which interstitial melts could no longer move, the trapped pore melts began to evolve via *in situ* fractional crystallization (Humphreys, 2009; Holness *et al.*, 2011). Permeability drops may be linked with inwardly migrating solidification fronts (Marsh, 1996). In OZ rocks this generated narrow Fe-rich rims on olivine primocrysts, evolved groundmass olivines, Fe–Ti enriched rims on clinopyroxene, sodic rims on plagioclase, and a cortège of minor phases (Fe–Ti oxides, mica, amphibole, and sulphides). The effects of *in situ* differentiation are most prominent just beneath the UBZ in the DZ, where clinopyroxene (Fig. 11) and plagioclase (Fig. 15) cores reach their most evolved compositions at a sandwich horizon. We tentatively suggest that this sandwich horizon developed late in the crystallization history of the LPS and post-dates the emplacement of the olivine slurry. This is based on the constraints provided by our data, which suggest that the LPS was only *c.* 40% solidified at the time of olivine slurry emplacement, rather than the >70% solidification required to produce the strongly evolved or fractionated mineral compositions seen in the sandwich horizon.

Implications for the differentiation and formation of cyclic–macrorhythmic layering in large layered intrusions

The LPS preserves first-order igneous layering that is similar to cyclic–macrorhythmic cumulate layering observed in large layered intrusions (Eales & Cawthorn, 1996; Wilson, 2012). The rapid cooling rate of the thin LPS preserves fine details of mineral textures and zoning that provide insights into the differentiation and layer-forming mechanisms. Similar mechanisms may also have operated in larger, more slowly cooled, magma chambers. We have presented evidence that suggests that the LPS OZ was emplaced as an olivine slurry near the base of a pre-existing gabbroic mush. The prominent layering seen in the LPS is in marked contrast to most dolerite-textured gabbroic sills. For example, the 150 m thick Beacon sill of the Ferrar suite in

Table 4. Representative plagioclase compositions

Type	Region	SiO_2	TiO_2	Al_2O_3	MgO	CaO	MnO	FeO	Na_2O	K_2O	BaO	SrO	Total	An
LCM														
Groundmass (166A1)	Core	51·2	0·08	29·7	0·27	13·9	0	1·12	3·6	0·2	0	0·07	100·3	67
LBZ														
Dendrite	Core	49·7	0·03	30·7	0·2	14·5	0	0·79	3·5	0·14	0	0·12	99·6	69
(166A3)	Mantle	48·6	0·09	31·1	0·1	14·9	0·05	0·92	3·2	0·15	0	0·08	99·3	71
	Rim	49·7	0·07	30·5	0·14	14·1	0	0·95	3·5	0·2	0	0·05	99·2	68
LOZ														
Interstitial	Core	49·2	0·01	30·4	0·35	14·9	0	0·76	3·2	0·12	0	0	99	71
(311B2)	Mantle	49·6	0·04	30·4	0·22	14·6	0	0·65	3·3	0·13	0	0·08	99	71
	Rim	49·9	0·1	30·3	0·17	14·2	0	0·9	3·6	0·18	0	0	99·3	68
MOZ														
Interstitial	Core	50	0·02	30·7	0·2	14·4	0	0·6	3·7	0·15	0	0·06	99·7	68
(167A3)	Mantle	51·5	0·08	29·8	0·18	13·4	0	0·68	4·1	0·23	0·03	0·06	100	63
	Rim	51·7	0·12	29·9	0·15	13	0	0·73	4·3	0·24	0	0·1	100·2	62
UOZ														
Interstitial	Core	52	0·05	30	0·15	13·6	0	0·69	3·9	0·19	0·03	0·08	100·8	65
(311B3)	Mantle	52·2	0·04	29·5	0·14	13·1	0	0·74	4·2	0·2	0	0·1	100·3	63
	Rim	53·2	0·09	28·9	0·1	12	0	0·71	4·7	0·35	0	0·09	100·1	57
CPZ														
Interstitial	Core	51·8	0·09	29·7	0·1	13·3	0	0·75	4·1	0·23	0	0·08	100·1	63
(311B4)	Mantle	51·9	0	29·6	0·1	13·3	0	0·79	3·9	0·23	0	0·06	100·1	64
	Rim	57·1	0·07	27·3	0·04	9·8	0·06	0·5	5·9	0·4	0·05	0·06	101·2	46
DZ														
Lath	Core	51·6	0·05	29·5	0·12	13·2	0·03	0·85	4·1	0·2	0	0·05	99·8	63
(167A9)	Mantle	50·7	0·14	29·5	0·13	13·1	0·05	0·82	4·1	0·2	0	0·1	98·9	63
	Rim	55·4	0·05	27·3	0·02	10·1	0	0·54	5·7	0·34	0·04	0·04	99·6	48
Cumulus	Core	48·9	0·04	31·7	0·2	16·2	0·07	0·55	2·5	0·09	0·06	0·05	100·4	78
lath	Mantle	49·5	0·03	31·3	0·2	15·5	0	0·56	2·7	0·09	0	0·07	100·1	75
(311B6)	Rim	51·7	0·01	29·6	0·2	13·4	0·1	0·6	3·7	0·34	0·03	0·04	99·6	65
Interstitial	Core	52·5	0·02	29·2	0·12	12·8	0	0·7	4·4	0·24	0	0·05	100	61
(167A12)	Mantle	54·1	0	28·6	0·08	11·8	0	0·6	4·8	0·33	0·07	0·06	100·5	56
	Rim	56·3	0	27·3	0·03	10·2	0·05	0·6	5·8	0·4	0·08	0	100·8	48
UBZ														
Dendrite	Core	50·8	0·02	30·4	0·15	14·2	0	0·79	3·5	0·18	0	0·07	100·1	69
(167A14)	Mantle	50·7	0·02	30·8	0·14	14·5	0	0·88	3·4	0·17	0·05	0·02	100·6	70
	Rim	50·3	0·04	31·2	0·1	15	0	0·97	3·1	0·18	0	0	100·8	72

Antarctica (Zieg & Marsh, 2012) shows only limited internal differentiation, and does not develop significant modal layering, even though it is seven times thicker than the *c*. 21 m LPS. Our data imply that the first-order cumulate layering structure (OZ–DZ duality) of the LPS was not formed by *in situ* closed-system differentiation of a single magma pulse, and that the LPS is a composite intrusion that records multiple intrusive pulses, a conclusion that is supported by our unpublished isotopic data (Beard *et al.*, in preparation; Hayes *et al.*, in preparation). Similar textural and phase relationships have been observed in the Lower, Critical and Main Zones of the Bushveld Complex, which have been linked to replenishment (Eales *et al.*, 1991; Mitchell *et al.*, 1998). Other intrusions and volcanic products also bear imprints of variable crystal cargoes, as shown by *in situ* isotopic modeling (Davidson *et al.*, 2007; Font *et al.*, 2008; Martin *et al.*, 2010).

Our results bear on a debate that has created very polarized views in the literature about how magma chambers form and differentiate. The DZ of the LPS (and most other sills of the Franklin suite) shows a D-shaped profile, with the development of an Fe–Ti-enriched zone (sandwich horizon) as a result of inward crystallization, much as argued by Shirley (1985) and others (Latypov, 2009). However, the OZ–DZ duality and S-shaped profile of the LPS as a whole appear to have formed through multiple injections, as advocated by Marsh (2004, 2013). We emphasize that the demonstration that some types of layering (in this instance, a basal olivine-rich layer) formed by emplacement of a crystal-charged slurry does not imply that magma cannot differentiate by *in situ* fractional crystallization.

The late emplacement of an olivine slurry in the LPS has other implications for magma chamber evolution. It seems axiomatic that such an event could occur only if the incoming slurry was driven by some type of magmatic overpressure. As the olivine-charged slurry is injected into a previously existing sill, space needs to be created to accommodate it. Either the sill inflates by floor subsidence and/or roof uplift, or an equivalent volume of pre-existing resident mush needs to be expelled. This remobilized gabbroic mush could be forced onwards to more distal zones as the overpressure allows the sill to expand laterally, it could be expelled into parasitic dykes, or it could be injected up-section to erupt at the surface if favourable structures are present to facilitate this. A multiple emplacement process similar to what we have documented in the LPS could also have operated in other basaltic provinces

and possibly other settings, explaining common glomerocrystic and disequilibrium crystal–melt assemblages (Larrea *et al.*, 2012; Passmore *et al.*, 2012; Leuthold *et al.*, 2014).

We also suggest the formation of a clinopyroxene-enriched layer at the interface between the OZ and DZ systems as a result of post-emplacement migration of interstitial melt. The possible development of the CPZ by mixing between OZ and DZ pore melts is similar to the mechanism of formation proposed for gabbros in the Rum intrusion (Bédard *et al.*, 1988) and pyroxenites in the Bay of Islands complex (Bédard, 1991), and is similar to that proposed for the formation of high-Mg# clinopyroxene in actively spreading mid-ocean ridge crust (Lissenberg & Dick, 2008), emphasizing the need to better understand the effects of igneous metasomatic processes during the solidification of igneous bodies.

CONCLUSIONS

The Lower Pyramid Sill (LPS) forms part of the sill-dominated Franklin magmatic plumbing system that is well exposed in the Minto Inlier of Victoria Island, Arctic Canada. The thin (*c.* 21 m) LPS is remarkably well layered, with a *c.* 7 m thick layer of olivine-cumulate melagabbro–feldspathic peridotite (OZ) that is capped by a thin (*c.* 1 m) layer of sector-zoned clinopyroxene-rich cumulate gabbro (CPZ) and a *c.* 10 m thick layer of sub-ophitic doleritic gabbro (DZ). The LPS OZ is subdivided based on textures into a pyroxene-poikilitic lower OZ (LOZ), a middle OZ (MOZ) and an upper OZ (UOZ), with MOZ and UOZ rocks characterized by abundant hopper olivine morphologies. The absence of systematic cryptic mineral compositional variations in the LPS OZ, the high proportions of modal olivine, the presence of reversely zoned olivines, and the variety of olivine morphologies within the OZ appear to preclude formation by *in situ* fractional crystallization of a single pulse of magma. The LPS OZ is best explained as the result of an intra-sill mixing event between an invading olivine slurry and a resident *c.* 40% solidified gabbroic mush. The dense olivine slurry was emplaced just above the largely solidified LBZ, and beneath the DZ. During its emplacement, the primitive, MgO-rich melts (*c.* 13–10 wt %) mixed with the more evolved resident mush (with *c.* 6 wt % MgO pore melt) that was already present in the LPS. Mixing produced a hybrid magma, with the highest proportions of DZ contaminant in the UOZ. As the OZ solidified, interstitial melt percolated up through the compacting olivine cumulate, forming hopper olivine (and local reversed zoning) and clinopyroxene. The CPZ that separates the OZ and DZ is dominated by enigmatic sector-zoned clinopyroxene that may have formed when hybrid melt expelled from the OZ reacted with more Fe-rich pore melt in the DZ. The DZ shows inward fractional crystallization trends culminating in a sandwich horizon just beneath the UBZ. Our differentiation model for the LPS implies that crystal-slurry replenishment and *in situ* differentiation were both involved in the development of the LPS OZ–DZ duality. Such a style of magma emplacement and differentiation may also be important in the construction of cyclic–macrorhythmic layering of larger layered intrusions.

ACKNOWLEDGEMENTS

This research was supported by the Geological Survey of Canada's GEM (Geomapping for Energy and Minerals) program. We thank the entire field crew involved during mapping on Victoria Island in 2010 and 2011 for a unique experience. We particularly thank Trent Dell'Oro, William MacDonald and Dylan Wales for help with sample collection, the helicopter and fixed-wing pilots for safely ferrying us and the rock cargo, Polar Shelf for logistical support, and the people of Ulukhaktok for their welcome. Marc Choquette at the University of Laval in Québec City is thanked for his help and support with the electron microprobe analyses. Discussions with Dick Naslund, John Maclennan, Wolfgang Maier and Michel Houlé helped improve the clarity of our arguments. Constructive reviews by Marian Holness, Bruce Marsh and George Bergantz, as well as editorial handling by Marjorie Wilson, are gratefully acknowledged. This is NRCAN/ESS contribution 20140232.

FUNDING

B.H. was supported by a Natural Environment Research Centre (NERC) research studentship (grant number NE/152787X/1).

SUPPLEMENTARY DATA

Supplementary data for this paper are available at *Journal of Petrology* online.

REFERENCES

Annen, C., Paulatto, M., Sparks, R. S. J., Minshull, T. A. & Kiddley, E. J. (2014). Quantification of the intrusive magma fluxes during magma chamber growth at Soufrière Hills volcano (Montserrat, Lesser Antilles). *Journal of Petrology* **55**, 529–548.

Arndt, N. T. (1977). Partitioning of nickel between olivine and ultrabasic and basic komatiite liquids. *Carnegie Institution of Washington Yearbook* **76**, 553–557.

Ballhaus, C. G. & Glikson, A. Y. (1989). Magma mixing and intraplutonic quenching in the Wingellina Hills Intrusion, Giles Complex, central Australia. *Journal of Petrology* **30**, 1443–1469.

Baragar, W. R. A. (1976). The Natkusiak basalts, Victoria Island, District of Franklin. *Report of Activities, Part A. Geological Survey of Canada Paper* **76-1 A**, 347–352.

Barnes, S. (1986). The effect of trapped liquid crystallization on cumulus mineral compositions in layered intrusions. *Contributions to Mineralogy and Petrology* **93**, 524–531.

Bédard, J. H. (1987). The development of compositional and textural layering in Archaean komatiites and in Proterozoic basaltic komatiites from Cape Smith, Quebec, Canada. In: Parsons, I. (ed.) *The Origin of Layering in Igneous Rocks.*

Proceedings of a NATO Workshop. Dordrecht: D. Reidel, pp. 399–418.

Bédard, J. H. (1991). Cumulate recycling and crustal evolution in the Bay of Islands ophiolite. *Journal of Geology* **99**, 225–249.

Bédard, J. H. (1993). Oceanic crust as a reactive filter: Synkinematic intrusion, hybridization, and assimilation in an ophiolitic magma chamber, western Newfoundland. *Geology* **21**, 77–80.

Bédard, J. H. (2010). Parameterization of the Fe = Mg exchange coefficient (Kd) between clinopyroxene and silicate melts. *Chemical Geology* **274**, 169–176.

Bédard, J. H., Sparks, R. S. J., Renner, R., Cheadle, M. J. & Hallworth, M. A. (1988). Peridotite sills and metasomatic gabbros in the Eastern Layered Series of the Rhum complex. *Journal of the Geological Society, London* **145**, 207–224.

Bédard, J. H., Naslund, H. R., Nabelek, P., Winpenny, A., Hryciuk, M., Macdonald, W., Hayes, B., Steigerwaldt, K., Hadlari, T., Rainbird, R., Dewing, K. & Girard, É. (2012). Fault-mediated melt ascent in a Neoproterozoic continental flood basalt province, the Franklin sills, Victoria Island, Canada. *Geological Society of America Bulletin* **124**, 723–736.

Bédard, J. H., Hayes, B., Hryciuk, M., Wing, B., Beard, C., Dell'Oro, T. A., Weis, D., Scoates, J. S., Williamson, N., Cousens, B., Naslund, H. R., MacDonald, W. & Nabelek, P. (2013). The Neoproterozoic Franklin Large Igneous Province on Victoria Island. *Geological Asssociation of Canada–Mineralogical Association of Canada Annual Meeting. Program with Abstracts* **35**, 82.

Bhattacharji, S. (1967). Mechanics of flow differentiation in ultramafic and mafic sills. *Journal of Geology* **75**, 101–112.

Boudreau, A. (1999). Fluid fluxing of cumulates: the J-M reef and associated rocks of the Stillwater Complex, Montana. *Journal of Petrology* **40**, 755–772.

Boudreau, A. E. & Philpotts, A. R. (2002). Quantitative modeling of compaction in the Holyoke flood basalt flow, Hartford Basin, Connecticut. *Contributions to Mineralogy and Petrology* **144**, 176–184.

Bowen, N. L. (1928). *The Evolution of Igneous Rocks*. Princeton, NJ: Princeton University Press.

Brophy, J. G., Whittington, C. S. & Young-Rok, P. (1999). Sector-zoned augite megacrysts in Aleutian high alumina basalts: implications for the conditions of basalt crystallization and the generation of calc-alkaline series magmas. *Contributions to Mineralogy and Petrology* **135**, 277–290.

Brown, G. M. (1956). The layered ultrabasic rocks of Rhum, Inner Hebrides. *Philosophical Transactions of the Royal Society of London, Series B* **240**, 1–53.

Carslaw, H. S. & Jaeger, J. C. (1959). *Conduction of Heat in Solids*. Oxford: Oxford University Press, 510 pp.

Cawthorn, R. G. & Walraven, F. (1998). Emplacement and crystallization time for the Bushveld Complex. *Journal of Petrology* **39**, 1669–1687.

Cawthorn, R. G. E. (1996). *Layered Intrusions*. Amsterdam: Elsevier.

Chakraborty, S. (1997). Rates and mechanisms of Fe–Mg interdiffusion in olivine at 980°–1300°C. *Journal of Geophysical Research: Solid Earth* **102**, 12317–12331.

Costa, F. & Dungan, M. (2005). Short time scales of magmatic assimilation from diffusion modeling of multiple elements in olivine. *Geology* **33**, 837–840.

Davidson, J. P., Morgan, D. J., Charlier, B. L. A., Harlou, R. & Hora, J. M. (2007). Microsampling and isotopic analysis of igneous rocks: Implications for the study of magmatic systems. *Annual Review of Earth and Planetary Sciences* **35**, 273–311.

Di Rocco, T., Freda, C., Gaeta, M., Mollo, S. & Dallai, L. (2012). Magma chambers emplaced in carbonate substrate: petrogenesis of skarn and cumulate rocks and implications for CO_2 degassing in volcanic areas. *Journal of Petrology* **53**, 2307–2332.

Donaldson, C. (1976). An experimental investigation of olivine morphology. *Contributions to Mineralogy and Petrology* **57**, 187–213.

Dungan, M. A. & Davidson, J. (2004). Partial assimilative recycling of the mafic plutonic roots of arc volcanoes: An example from the Chilean Andes. *Geology* **32**, 773–776.

Eales, H. V. & Cawthorn, R. G. (1996). The Bushveld Complex. In: Cawthorn, R. G. (ed.) *Layered Intrusions. Developments in Petrology* **15**, 181–229.

Eales, H. V., Maier, W. D. & Teigler, B. (1991). Corroded plagioclase feldspar inclusions in orthopyroxene and olivine of the Lower and Critical Zones, Western Bushveld Complex. *Mineralogical Magazine* **55**, 479–486.

Field, L., Blundy, J., Calvert, A. & Yirgu, G. (2013). Magmatic history of Dabbahu, a composite volcano in the Afar Rift, Ethiopia. *Geological Society of America Bulletin* **125**, 128–147.

Font, L., Davidson, J. P., Pearson, D. G., Nowell, G. M., Jerram, D. A. & Ottley, C. J. (2008). Sr and Pb isotope micro-analysis of plagioclase crystals from Skye lavas: An insight into open-system processes in a flood basalt province. *Journal of Petrology* **49**, 1449–1471.

Gaeta, M., Di Rocco, T. & Freda, C. (2009). Carbonate assimilation in open magmatic systems: the role of melt-bearing skarns and cumulate-forming processes. *Journal of Petrology* **50**, 361–385.

Garcia, M. O., Pietruszka, A. J. & Rhodes, J. M. (2003). A petrologic perspective of Kīlauea volcano's summit magma reservoir. *Journal of Petrology* **44**, 2313–2339.

Gibb, F. G. F. & Henderson, C. M. B. (2006). Chemistry of the Shiant Isles Main Sill, NW Scotland, and wider implications for the petrogenesis of mafic sills. *Journal of Petrology* **47**, 191–230.

Ginibre, C. & Wörner, G. (2007). Variable parent magmas and recharge regimes of the Parinacota magma system (N. Chile) revealed by Fe, Mg and Sr zoning in plagioclase. *Lithos* **98**, 118–140.

Gorring, M. L. & Naslund, H. R. (1995). Geochemical reversals within the lower 100 m of the Palisades sill, New Jersey. *Contributions to Mineralogy and Petrology* **119**, 263–276.

Grove, T. L., Baker, M. B. & Kinzler, R. J. (1984). Coupled CaAl–NaSi diffusion in plagioclase feldspar: Experiments and applications to cooling rate speedometry. *Geochimica et Cosmochimica Acta* **48**, 2113–2121.

Gunn, B. M. (1966). Modal and element variation in Antarctic tholeiites. *Geochimica et Cosmochimica Acta* **30**, 881–920.

Hart, S. R. & Davis, K. E. (1978). Nickel partitioning between olivine and silicate melt. *Earth and Planetary Science Letters* **40**, 203–219.

Heaman, L. M., LeCheminant, A. N. & Rainbird, R. H. (1992). Nature and timing of Franklin igneous events, Canada: Implications for a Late Proterozoic mantle plume and the break-up of Laurentia. *Earth and Planetary Science Letters* **109**, 117–131.

Holness, M. B., Tegner, C., Nielsen, T. F. D., Stripp, G. & Morse, S. A. (2007). A textural record of solidification and cooling in the Skaergaard intrusion, East Greenland. *Journal of Petrology* **48**, 2359–2377.

Holness, M. B., Stripp, G., Humphreys, M. C. S., Veksler, I. V., Nielsen, T. F. D. & Tegner, C. (2011). Silicate liquid immiscibility within the crystal mush: late-stage magmatic microstructures in the Skaergaard intrusion, East Greenland. *Journal of Petrology* **52**, 175–222.

Humphreys, M. C. S. (2009). Chemical evolution of intercumulus liquid, as recorded in plagioclase overgrowth rims

from the Skaergaard intrusion. *Journal of Petrology* **50**, 127–145.

Humphreys, M. C. S., Blundy, J. D. & Sparks, R. S. J. (2006). Magma evolution and open-system processes at Shiveluch Volcano: Insights from phenocryst zoning. *Journal of Petrology* **47**, 2303–2334.

Hunter, R. H. (1996). Texture development in cumulate rocks. In: Cawthorn, R. G. (ed.) *Developments in Petrology* **15**, 77–101.

Huppert, H. E. & Sparks, R. S. J. (1980). The fluid dynamics of a basaltic magma chamber replenished by influx of hot, dense ultrabasic magma. *Contributions to Mineralogy and Petrology* **75**, 279–289.

Irvine, T. N. (1977). Origin of chromitite layers in the Muskox intrusion and other stratiform intrusions: A new interpretation. *Geology* **5**, 273–277.

Irvine, T. N. & Smith, C. H. (1967). The ultramafic rocks of the Muskox intrusion, Northwest Territories, Canada. In: Wyllie, P. J. (ed.) *Ultramafic and Related Rocks*. New York: John Wiley, pp. 38–49.

Jefferson, C. W., Nelson, W. E., Kirkham, R. V., Reedman, J. H. & Scoates, R. F. J. (1985). Geology and copper occurrences of the Natkusiak Basalts, Victoria Island, District of Franklin. Current Research, Part A. *Geological Survey of Canada Paper* **85-1A**, 203–214.

Jones, D. S., Maloof, A. C., Hurtgen, M. T., Rainbird, R. H. & Schrag, D. P. (2010). Regional and global chemostratigraphic correlation of the early Neoproterozoic Shaler Supergroup, Victoria Island, Northwestern Canada. *Precambrian Research* **181**, 43–63.

Larrea, P., França, Z., Lago, M., Widom, E., Galé, C. & Ubide, T. (2012). Magmatic processes and the role of antecrysts in the genesis of Corvo Island (Azores Archipelago, Portugal). *Journal of Petrology* **54**, 769–793.

Latypov, R. (2009). Testing the validity of the petrological hypothesis 'no phenocrysts, no post-emplacement differentiation'. *Journal of Petrology* **50**, 1047–1069.

Leuthold, J., Müntener, O., Baumgartner, L. P. & Putlitz, B. (2014). Petrological constraints on the recycling of mafic crystal mushes and intrusion of braided sills in the Torres del Paine mafic complex (Patagonia). *Journal of Petrology* **55**, 917–949.

Lissenberg, C. J. & Dick, H. J. B. (2008). Melt–rock reaction in the lower oceanic crust and its implications for the genesis of mid-ocean ridge basalt. *Earth and Planetary Science Letters* **271**, 311–325.

Macdonald, F. A., Schmitz, M. D., Crowley, J. L., Roots, C. F., Jones, D. S., Maloof, A. C., Strauss, J. V., Cohen, P. A., Johnston, D. T. & Schrag, D. P. (2010). Calibrating the Cryogenian. *Science* **327**, 1241–1243.

Marsh, B. D. (1996). Solidification fronts and magmatic evolution. *Mineralogical Magazine* **60**, 5–40.

Marsh, B. D. (2004). A magmatic mush column Rosetta Stone: the McMurdo Dry Valleys, Antarctica. *EOS Transactions, American Geophysical Union* **85**, 497.

Marsh, B. D. (2013). On some fundamentals of igneous petrology. *Contributions to Mineralogy and Petrology* **166**, 665–690.

Martin, V. M., Davidson, J., Morgan, D. & Jerram, D. A. (2010). Using the Sr isotope compositions of feldspars and glass to distinguish magma system components and dynamics. *Geology* **38**, 539–542.

Matzen, A. K., Baker, M. B., Beckett, J. R. & Stolper, E. M. (2011). Fe–Mg partitioning between olivine and high-magnesian melts and the nature of Hawaiian parental liquids. *Journal of Petrology* **52**, 1243–1263.

McBirney, A. R. (1996). The Skaergaard Intrusion. In: Cawthorn, R. G. (ed.) Layered Intrusions. *Developments in Petrology* **15**, 147–180.

McDonald, I. & Viljoen, K. S. (2006). Platinum-group element geochemistry of mantle eclogites: a reconnaissance study of xenoliths from the Orapa kimberlite, Botswana. *Applied Earth Science* **115**, 81–93.

Meurer, W. P. & Boudreau, A. E. (1998). Compaction of igneous cumulates Part I: Geochemical consequences for cumulates and liquid fractionation trends. *Journal of Geology* **106**, 281–292.

Mitchell, A. A., Eales, H. V. & Krueger, F. J. (1998). Magma replenishment, and the significance of poikilitic textures, in the Lower Main Zone of the western Bushveld Complex, South Africa. *Mineralogical Magazine* **62**, 435–450.

Morgan, D. J., Blake, S., Rogers, N. W., De Vivo, B., Rolandi, G. & Davidson, J. P. (2006). Magma chamber recharge at Vesuvius in the century prior to the eruption of A.D. 79. *Geology* **34**, 845–848.

Morse, S. A. (1984). Cation diffusion in plagioclase feldspar. *Science* **225**, 504–505.

Müller, T., Dohmen, R., Becker, H. W., Heege, J. & Chakraborty, S. (2013). Fe–Mg interdiffusion rates in clinopyroxene: experimental data and implications for Fe–Mg exchange geothermometers. *Contributions to Mineralogy and Petrology* **166**, 1563–1576.

Murphy, M. D., Sparks, R. S. J., Barclay, J., Carroll, M. R. & Brewer, T. S. (2000). Remobilization of andesite magma by intrusion of mafic magma at the Soufrière Hills volcano, Montserrat, West Indies. *Journal of Petrology* **41**, 21–42.

Nabelek, P. I., Bédard, J. H., Hryciuk, M. & Hayes, B. (2013). Short-duration contact metamorphism of calcareous sedimentary rocks by Neoproterozoic Franklin gabbro sills and dykes on Victoria Island, Canada. *Journal of Metamorphic Geology* **31**, 205–220.

Nakamura, Y. (1973). Origin of sector-zoning of igneous clinopyroxenes. *American Mineralogist* **58**, 986–990.

Namur, O., Charlier, B., Toplis, M. J., Higgins, M. D., Liégeois, J.-P. & Vander Auwera, J. (2010). Crystallization sequence and magma chamber processes in the ferrobasaltic Sept Iles layered intrusion, Canada. *Journal of Petrology* **51**, 1203–1236.

Naslund, H. R. (1989). Petrology of the Basistoppen Sill, East Greenland: a calculated magma differentiation trend. *Journal of Petrology* **30**, 299–319.

Naslund, H. R., Bédard, J. H., Steigerwaldt, K. & Dye, D. (2013). Origin of S and M and reversed S and M shaped profiles in two Proterozoic mafic sills from the Franklin magmatic event, Victoria Island, NWT, Canada. *Geophysical Research Abstracts* **15**, EGU2013-10006-3.

O'Driscoll, B., Donaldson, C. H., Troll, V. R., Jerram, D. A. & Emeleus, C. H. (2007). An origin for harrisitic and granular olivine in the Rum Layered Suite, NW Scotland: a crystal size distribution study. *Journal of Petrology* **48**, 253–270.

O'Hara, M. J. (1977). Geochemical evolution during fractional crystallization of a periodically refilled magma chamber. *Nature* **266**, 503–507.

Okulitch, A. V. (1992). Geological Atlas, Horton River, Franklin–Mackenzie. *Geological Survey of Canada Map* NR-9/10/11/12-G, scale 1:1,000,000, sheet 1 of 3.

Onuma, K. & Tohara, T. (1983). Effect of chromium on phase relations in the join forsterite–anorthite–diopside in air at 1 atm. *Contributions to Mineralogy and Petrology* **84**, 174–181.

Parsons, I. (ed.) (1987). *Origins of Igneous Layering. NATO ASI Series C, Mathematical and Physical Sciences* **196**, 666 pp.

Passmore, E., Maclennan, J., Fitton, G. & Thordarson, T. (2012). Mush disaggregation in basaltic magma chambers: evidence from the AD 1783 Laki eruption. *Journal of Petrology* **53**, 2593–2623.

Paterson, S. R. (2009). Magmatic tubes, pipes, troughs, diapirs, and plumes: Late-stage convective instabilities resulting in compositional diversity and permeable networks in crystal-rich magmas of the Tuolumne batholith, Sierra Nevada, California. *Geosphere* **5**, 496–527.

Philpotts, A. R., Shi, J. & Brustman, C. (1998). Role of plagioclase crystal chains in the differentiation of partly crystallized basaltic magma. *Nature* **395**, 343–346.

Puffer, J. H., Block, K. A. & Steiner, J. C. (2009). *Transmission of Flood Basalts through a Shallow Crustal Sill and the Correlation of Sill Layers with Extrusive Flows: The Palisades Intrusive System and the Basalts of the Newark Basin, New Jersey, U.S.A*. Chicago, IL: University of Chicago Press. *Journal of Geology* **117**, 139–155.

Rainbird, R. H., Jefferson, C. W. & Young, G. M. (1996). The early Neoproterozoic sedimentary Succession B of northwestern Laurentia: Correlations and paleogeographic significance. *Geological Society of America Bulletin* **108**, 454–470.

Reubi, O. & Blundy, J. (2008). Assimilation of plutonic roots, formation of high-K 'exotic' melt inclusions and genesis of andesitic magmas at Volcán De Colima, Mexico. *Journal of Petrology* **49**, 2221–2243.

Roeder, P. L. & Emslie, R. F. (1970). Olivine–liquid equilibrium. *Contributions to Mineralogy and Petrology* **29**, 275–289.

Shirley, D. N. (1985). Compaction of igneous cumulates. *Journal of Geology* **94**, 795–809.

Simkin, T. (1967). Flow differentiation in the picritic sills of North Skye. In: Wyllie, P. J. (ed.) *Ultramafic and Related Rocks*. New York: John Wiley, pp. 64–69.

Smewing, J. D. (1981). Mixing characteristics and compositional differences in mantle-derived melts beneath spreading axes; evidence from cyclically layered rocks in the ophiolite of North Oman. *Journal of Geophysical Research* **86**, 2645–2659.

Sparks, R. S. J., Sigurdsson, H. & Wilson, L. (1977). Magma mixing: a mechanism of triggering acid explosive eruptions. *Nature* **267**, 315–318.

Tait, S. R. (1985). Fluid dynamic and geochemical evolution of cyclic unit 10, Rhum, Eastern Layered Series. *Geological Magazine* **122**, 469–484.

Tegner, C. (1997). Iron in plagioclase as a monitor of the differentiation of the Skaergaard intrusion. *Contributions to Mineralogy and Petrology* **128**, 45–51.

Tegner, C., Wilson, J. R. & Brooks, C. K. (1993). Intraplutonic quench zones in the Kap Edvard Holm layered gabbro complex, East Greenland. *Journal of Petrology* **34**, 681–710.

Tepley, F. J., Davidson, J. P., Tilling, R. I. & Arth, J. G. (2000). Magma mixing, recharge and eruption histories recorded in plagioclase phenocrysts from El Chichón volcano, Mexico. *Journal of Petrology* **41**, 1397–1411.

Thomson, D., Rainbird, R. H. & Dix, G. (2014). Architecture of a Neoproterozoic intracratonic carbonate ramp succession: Wynniatt Formation, Amundsen Basin, Arctic Canada. *Sedimentary Geology* **299**, 119–138.

Thorsteinsson, R. & Tozer, E. T. (1962). Banks, Victoria and Stefansson Islands, Arctic Archipelago. *Geological Survey of Canada Memoir* **330**, 85 Pp.

Usselman, T. M. & Hodge, D. S. (1978). Thermal control of low-pressure fractionation processes. *Journal of Volcanology and Geothermal Research* **4**, 265–281.

van Acken, D., Thomson, D., Rainbird, R. H. & Creaser, R. A. (2013). Constraining the depositional history of the Neoproterozoic Shaler Supergroup, Amundsen Basin, NW Canada: Rhenium–osmium dating of black shales from the Wynniatt and Boot Inlet Formations. *Precambrian Research* **236**, 124–131.

Wager, L. R. & Brown, G. M. (1968). *Layered Igneous Rocks*. Edinburgh: Oliver & Boyd.

Wager, L. R. & Deer, W. A. (1939). *Geological investigations in East Greenland Part III. The petrology of the Skaergaard Intrusion, Kangerdlugssuaq, East Greenland. Meddelelser om Grønland* **105**, 352 pp.

Wallace, G. S. & Bergantz, G. W. (2002). Wavelet-based correlation (WBC) of zoned crystal populations and magma mixing. *Earth and Planetary Science Letters* **202**, 133–145.

Welsch, B., Faure, F., Famin, V., Baronnet, A. & Bachèlery, P. (2012). Dendritic crystallization: a single process for all the textures of olivine in basalts? *Journal of Petrology* **54**, 539–574.

Williamson, N., Bédard, J. H., Ootes, L., Rainbird, R., Cousens, B. & Zagorevski, A. (2013). Volcanostratigraphy and significance of the southern lobe Natkusiak Formation flood basalts, Victoria Island, Northwest Territories. *Geological Survey of Canada, Current Research* **2013–16**, 13 pp.

Wilson, A. H. (2012). A chill sequence to the Bushveld Complex: insight into the first stage of emplacement and implications for the parental magmas. *Journal of Petrology* **53**, 1123–1168.

Zieg, M. J. & Marsh, B. D. (2012). Multiple reinjections and crystal-mush compaction in the Beacon Sill, McMurdo Dry Valleys, Antarctica. *Journal of Petrology* **53**, 2567–2591.